Planck 2013 results. VIII. HFI photometric calibration and mapmaking

Planck Collaboration,; Ade, P. A. R.; Aghanim, N.; Armitage-Caplan, C.; Arnaud, M.; Ashdown, M.; Atrio-Barandela, F.; Aumont, J.; Baccigalupi, C.; Banday, A. J.

Total number of authors:
226

Published in:
ArXiv Astrophysics e-prints

Publication date:
2013

Document Version
Publisher's PDF, also known as Version of record

Astronomy & Astrophysics manuscript no. calibration
March 22, 2013

Planck 2013 results. VIII. HFI photometric calibration and mapmaking

Planck Collaboration: P. A. R. Ade[81], N. Aghanim[55], C. Armitage-Caplan[86], M. Arnaud[68], M. Ashdown[64,6], F. Atrio-Barandela[18], J. Aumont[55], C. Baccigalupi[80], A. J. Banday[89,10], R. B. Barreiro[61], E. Battaner[90], K. Benabed[56,88], A. Benoît[53], A. Benoit-Lévy[23,56,88], J.-P. Bernard[10], M. Bersanelli[32,46], B. Bertincourt[55], P. Bielewicz[89,10,80], J. Bobin[68], J. J. Bock[62,11], J. R. Bond[9], J. Borrill[14,83], F. R. Bouchet[56,88], F. Boulanger[55], M. Bridges[64,6,59], M. Bucher[1], C. Burigana[45,30], J.-F. Cardoso[69,1,56], A. Catalano[70,66], A. Challinor[59,64,12], A. Chamballu[68,15,55], R.-R. Chary[52], X. Chen[52], L.-Y Chiang[58], H. C. Chiang[25,7], P. R. Christensen[76,35], S. Church[85], D. L. Clements[51], S. Colombi[56,88], L. P. L. Colombo[22,62], C. Combet[70], F. Couchot[65], A. Coulais[66], B. P. Crill[62,77], A. Curto[6,61], F. Cuttaia[45], L. Danese[80], R. D. Davies[63], P. de Bernardis[31], A. de Rosa[45], G. de Zotti[42,80], J. Delabrouille[1], J.-M. Delouis[56,88], F.-X. Désert[49], C. Dickinson[63], J. M. Diego[61], H. Dole[55,54], S. Donzelli[46], O. Doré[62,11], M. Douspis[55], X. Dupac[37], G. Efstathiou[59], T. A. Enßlin[73], H. K. Eriksen[60], C. Filliard[65], F. Finelli[45,47], O. Forni[89,10], M. Frailis[44], E. Franceschi[45], S. Galeotta[44], K. Ganga[1], M. Giard[89,10], G. Giardino[38], Y. Giraud-Héraud[1], J. González-Nuevo[61,80], K. M. Górski[62,92], S. Gratton[64,59], A. Gregorio[33,44], A. Gruppuso[45], F. K. Hansen[60], D. Hanson[74,62,9], D. Harrison[59,64], G. Helou[11], S. Henrot-Versillé[65], C. Hernández-Monteagudo[13,73], D. Herranz[61], S. R. Hildebrandt[11], E. Hivon[56,88], M. Hobson[6], W. A. Holmes[62], A. Hornstrup[16], W. Hovest[73], K. M. Huffenberger[91], T. R. Jaffe[89,10], A. H. Jaffe[51], W. C. Jones[25], M. Juvela[24], E. Keihänen[24], R. Keskitalo[21,14], T. S. Kisner[72], R. Kneissl[36,8], J. Knoche[73], L. Knox[26], M. Kunz[17,55,3], H. Kurki-Suonio[24,40], G. Lagache[55], J.-M. Lamarre[66], A. Lasenby[6,64], R. J. Laureijs[38], C. R. Lawrence[62], M. Le Jeune[1], E. Lellouch[67], R. Leonardi[37], C. Leroy[55,89,10], J. Lesgourgues[87,79], M. Liguori[29], P. B. Lilje[60], M. Linden-Vørnle[16], M. López-Caniego[61], P. M. Lubin[27], J. F. Macías-Pérez[70], B. Maffei[63], N. Mandolesi[45,5,30], M. Maris[44], D. J. Marshall[68], P. G. Martin[9], E. Martínez-González[61], S. Masi[31], S. Matarrese[29], F. Matthai[73], L. Maurin[1], P. Mazzotta[34], P. McGehee[52], P. R. Meinhold[27], A. Melchiorri[31,48], L. Mendes[37], A. Mennella[32,46], M. Migliaccio[59,64], S. Mitra[50,62], M.-A. Miville-Deschênes[55,9], A. Moneti[56], L. Montier[89,10], R. Moreno[67], G. Morgante[45], D. Mortlock[51], D. Munshi[81], J. A. Murphy[75], P. Naselsky[76,35], F. Nati[31], P. Natoli[30,4,45], C. B. Netterfield[19], H. U. Nørgaard-Nielsen[16], F. Noviello[63], D. Novikov[51], I. Novikov[76], S. Osborne[85], C. A. Oxborrow[16], F. Paci[80], L. Pagano[31,48], F. Pajot[55], R. Paladini[52], D. Paoletti[45,47], B. Partridge[39], F. Pasian[44], G. Patanchon[1], O. Perdereau[65]⋆, L. Perotto[70], F. Perrotta[80], F. Piacentini[31], M. Piat[1], E. Pierpaoli[22], D. Pietrobon[62], S. Plaszczynski[65], E. Pointecouteau[89,10], G. Polenta[4,43], N. Ponthieu[55,49], L. Popa[57], T. Poutanen[40,24,2], G. W. Pratt[68], G. Prézeau[11,62], S. Prunet[56,88], J.-L. Puget[55], J. P. Rachen[20,73], M. Reinecke[73], M. Remazeilles[55,1], C. Renault[70], S. Ricciardi[45], T. Riller[73], I. Ristorcelli[89,10], G. Rocha[62,11], C. Rosset[1], G. Roudier[1,66,62], B. Rusholme[52], D. Santos[70], G. Savini[78], E. P. S. Shellard[12], L. D. Spencer[81], J.-L. Starck[68], V. Stolyarov[6,64,84], R. Stompor[1], R. Sudiwala[81], R. Sunyaev[73,82], F. Sureau[68], D. Sutton[59,64], A.-S. Suur-Uski[24,40], J.-F. Sygnet[56], J. A. Tauber[38], D. Tavagnacco[44,33], S. Techene[56], L. Terenzi[45], M. Tomasi[46], M. Tristram[65], M. Tucci[17,65], G. Umana[41], L. Valenziano[45], J. Valiviita[40,24,60], B. Van Tent[71], P. Vielva[61], F. Villa[45], N. Vittorio[34], L. A. Wade[62], B. D. Wandelt[56,88,28], D. Yvon[15], A. Zacchei[44], A. Zonca[27]

(Affiliations can be found after the references)

Received XX, 2013; accepted XX, 2023

Abstract

This paper describes the processing applied to the *Planck* High Frequency Instrument (HFI) cleaned time-ordered information to produce photometrically calibrated maps. HFI observes the sky over a broad range of frequencies, from 100 to 857 GHz. To get the best accuracy on the calibration on such a large range, two different photometric calibration schemes have to be used. The 545 and 857 GHz data are calibrated using Uranus and Neptune flux density measurements, compared with models of their atmospheric emissions to calibrate the data. The lower frequencies (below 353 GHz) are calibrated using the cosmological microwave background dipole. One of the components of this anisotropy results from the orbital motion of the satellite in the Solar System, and is therefore time-variable. Photometric calibration is thus tightly linked to mapmaking, which also addresses low frequency noise removal. The 2013 released HFI data show some evidence for apparent gain variations of the HFI bolometers' detection chain. These variations were identified by comparing observations taken more than one year apart in the same configuration. We developed an effective correction to limit its effect on calibration, and assess its accuracy. We present several methods used to estimate the precision of the photometric calibration. We distinguish relative (from one detector to another, or from one frequency to another) and absolute uncertainties. In both cases, we found that these uncertainties range from a few 10^{-3} to several per cents from 100 to 857 GHz. We describe the pipeline producing the maps from the HFI timelines, based on the photometric calibration parameters and we detail the scheme used to a posteriori set the zero level of the maps. We also briefly discuss the cross-calibration between HFI and the SPIRE instrument on board *Herschel*. We finally summarize the basic characteristics of the set of the HFI maps from the 2013 *Planck* data release.

Key words. Cosmology: observations – Cosmic background radiation – Surveys – methods: data analysis

⋆ Corresponding author: O. Perdereau perdereau@lal.in2p3.fr

1. Introduction

This paper, one of a set associated with the 2013 release of data from the *Planck* mission[1] (Planck Collaboration I 2013), describes the processing applied to *Planck* High Frequency Instrument (HFI) cleaned Time-Ordered Information (TOI) to produce photometric calibrated sky maps

Photometric calibration in astronomy relies most often on relative calibration using a few reference sources. New frequency ranges have to establish their reference sources. The millimetre/sub-millimetre is in an unique situation as the Cosmic Microwave Background (CMB) contains 95 % of the cosmic background power. The spectral energy distribution (SED) of this isotropic background was measured very successfully and very accurately by the *COBE*-FIRAS experiment, and is by far the most accurate photometric calibration reference (Mather et al. 1999). The measurement by *COBE*-FIRAS was not a direct measurement of the SED but a null experiment with a double differential measurement between the sky on one arm of the polarising interferometer and a black body on the other arm, and a second measurement replacing the sky by a second black body. When both black bodies are at a temperature very close to that of the CMB, the measurement is the SED of the very small difference between the measured emissivity and the CMB.

The most precise calibrator that can be used in CMB experiments is thus the CMB dipole anisotropy produced by the observer's motion in the Solar system, which is very precisely known. The accuracy to which this calibrator is known is determined by that of the CMB temperature measured by FIRAS. At high-frequency ($\geq$ 500 GHz), the dipole become too faint with respect to the Galactic foregrounds to give an accurate calibration. However, those Galactic foregrounds, also measured by FIRAS (Wright et al. 1991; Reach et al. 1995; Fixsen et al. 1998; Lagache et al. 1999), could be used to calibrate diffuse emission. For FIRAS measurements in the sub-millimetre, the black bodies were set to higher temperatures. The foreground signal is steeply rising with frequency while the reference black body emission is at best constant or falling with frequency. The measurement is no longer a null detection. It depends on the gains, linearity, and filters transmission (there are two measurement channels in FIRAS, a high-frequency and a low-frequency one overlapping around 600 GHz). The only alternative to using FIRAS data to calibrate the data in the millimetre/sub-millimetre is to use the planet measurements. Primary calibrators are the planets Mars, Uranus or Neptune (used either for ground-based or space-based experiments, e.g., SCUBA and *Herschel*-SPIRE). However, they have not yet been measured or modelled with better than 5 % accuracy (Moreno 2010).

As *Planck*-HFI main science goals are based on the analysis of diffuse emissions, we wanted the primary absolute calibration of the *Planck*-HFI instrument to be an extended source calibration. At low frequencies, we use the measurement of the Solar dipole parameters from *WMAP* (Hinshaw et al. 2009) in all our analysis, summarized in Table 1. At high frequencies, although we used the Galactic emission as measured by FIRAS for the calibration of the *Planck* early papers (Planck HFI Core Team 2011a), we now have a better accuracy using planet measurements. Thus, the absolute calibration of the two high-frequency channels is done using Uranus and Neptune.

Table 1. Parameters of the Solar dipole, as measured in Hinshaw et al. (2009)

Amplitude	3.355 ± 0.008	[mK_{CMB}]
Galactic longitude	263.99 ± 0.14	[°]
Galactic colatitude	48.26 ± 0.03	[°]

At all frequencies, the zero levels of the maps are obtained by assuming no Galactic emission at zero gas column density, and adding the Comic Infrared Background (CIB) mean level.

We describe in this paper the photometric calibration and mapmaking applied to the 2013 *Planck* HFI data release. We first give our calibration conventions (Sect. 2), and summarize the mapmaking procedure (Sect. 3). We outline the calibration method used for the CMB-dominated channels (100 to 353 GHz) in Sect. 4. In Sect. 4.2, we show unexpected response variations with time for most of the low-frequency bolometers, and present an effective correction in Sect. 4.3. We then detail the calibration for the 545 and 857 GHz channels (Sect. 5) and describe how the zero level of the maps can be fixed (Sect. 6). We finally quantify the accuracy of the photometric calibration, and give basic characteristics of the delivered maps in Sect. 7. A conclusion is given in Sect. 8.

2. Calibration philosophy and conventions

2.1. Colour corrections

Whatever the origin of the calibrator (on the sky or an internal black body), the calibration is done with a source of known spectral energy distribution (SED). Except for CMB anisotropies, in general, the observed source has not the same SED as the calibration source. Although the simplest way to express the calibration is to give the response as a function of the power falling onto the detector, we usually use a secondary expression of the measurements as spectral densities. This allows us to compare the measurements with others and with models. Spectral densities are either an intensity (W m^{-2} sr^{-1} Hz^{-1}) for brightness or flux densities (W m^{-2} Hz^{-1}) for unresolved sources, expressed at a reference frequency such that the power integrated in the spectral bandpass and throughout is equal to the measured power. The intensity (or flux density) is thus always linked to the choice of both a reference frequency and an assumed SED.

Assuming a different SED than the reference one requires a color correction. Following the *IRAS* convention, the spectral intensity data I_ν, are often expressed at fixed nominal frequencies, assuming the source spectrum is νI_ν = cst (i.e., constant intensity per logarithmic frequency interval, so-called "ref_SED"). The color correction factor cc is defined such that:

$$I_{\nu_0}(\text{act\_SED}) = \frac{I_{\nu_0}(\text{ref\_SED})}{cc} \quad (1)$$

where I_{ν_0}(act_SED) is the actual specific intensity of the sky at frequency ν_0, I_{ν_0}(ref_SED) is the corresponding value given with the *IRAS* (Neugebauer et al. 1984) or DIRBE (Silverberg et al. 1993) convention[2] and ν_0 is the frequency corresponding to the

[1] *Planck* (http://www.esa.int/Planck) is a project of the European Space Agency (ESA) with instruments provided by two scientific consortia funded by ESA member states (in particular the lead countries France and Italy), with contributions from NASA USA) and telescope reflectors provided by a collaboration between ESA and a scientific consortium led and funded by Denmark.

[2] The DIRBE and IRAS data products give $I_{\nu_0}(\nu I_\nu = cst)$

nominal wavelength of the considered band. With these definitions:

$$cc = \frac{\int (I_\nu/I_{\nu_0})_{\rm act\_SED} R_\nu d\nu}{\int (\nu_0/\nu) R_\nu d\nu} \quad (2)$$

where $(I_\nu/I_{\nu_0})_{\rm act\_SED}$ is the actual specific intensity of the sky normalised to the intensity at frequency ν_0 and R_ν is the spectral response (Planck Collaboration IX 2013).

2.2. CMB dipole conventions

The CMB anisotropies are calibrated on the CMB dipoles (and inter-calibrated on the CMB anisotropies). The CMB temperature gives a calibration only for a CMB anisotropy SED. CMB anisotropies are thus referred to by a δT in $K_{\rm CMB}$. For the other astrophysical components with a different SED, this calibration has to be re-expressed as intensity at the reference frequencies for the *IRAS* convention. At high frequency, the calibration is done on astrophysical sources, and is thus only expressed as an intensity at the reference frequency for the reference SED. Maps are thus given in MJy sr^{-1} for the *IRAS* convention. Again, assuming a different SED than the reference one requires a color correction.

For HFI calibration at low frequency, unlike what is done for the LFI calibration (Planck Collaboration V 2013), we used the classical approximation of the dipole anisotropy:

$$\frac{\delta T}{T} = \beta \cos\theta \quad (3)$$

where $\beta = v/c$ is the ratio between the observer velocity v and the speed of light. For the CMB dipole, $\beta \sim 1.2 \times 10^{-3}$. The leading order term of the relativistic corrections is $\beta^2(\cos^2\theta - 1/2)$ (Kamionkowski & Knox 2003). The amplitude of this correction is of $\pm 1/2\beta^2$, so using this quadrupole term has a relative amplitude of 0.6×10^{-3} with respect to the classical term of Eq. 3. However, this quadrupole is only coupled to the dipole when masking part of the sky, which is small ($\sim 10\%$) in our calibration scheme, so the real bias must be smaller. Indeed, when using as calibrator the orbital dipole, which is a factor ~ 10 smaller than the Solar dipole, Tristram et al. (2011) showed that using the classical approximation leads to a relative bias as small as 6×10^{-6}. Given the level of systematic uncertainties we estimate in the following, it is therefore legitimate, and much simpler, to use the classical approximation of the Solar dipole anisotropy.

2.3. Far Side Lobes

The far side lobes (FSL) impact on HFI data is discussed in details in Planck Collaboration VII (2013). We present only a summary of their impact on calibration in this section.

FSL may affect the calibration determination in different ways. The power measured by our detectors p_{mes} may be schematically written as:

$$p_{mes} = g(S_{ML} + S_{FSL}) + noise \quad (4)$$

where S_{ML} denotes the sky signal incoming through the main lobe and S_{FSL} that coming through the far side ones. We also note f_{FSL} the fraction of power going into the FSL. For the planet photometry, some level of knowledge of f_{FSL} is needed to correctly compare the reconstructed flux with the planet brightness. However, the relative FSL power is lower than 0.3 % (Tauber et al. 2010) for all HFI frequencies, which is well below the systematic uncertainties of the planet emission models we are using, which are ~ 5 % (see Sect. 5). Therefore FSL can safely be ignored in the 545 and 857 GHz calibration analyses.

For the diffuse emission calibration on the CMB dipole at low HFI frequencies, we use a fit of the observed data to the Solar dipole as measured by the WMAP team (Hinshaw et al. 2009), as detailed in Sect. 4, without convolving it with a beam model, which is different from what is done in the LFI calibration pipeline (Planck Collaboration V 2013). To clarify the consequences of this choice, we have to examine in details the FSL signal. Far side lobes signal may be decomposed at first order into three main components, depending on their optical paths: the primary, secondary and baffle spillovers, named PR and SR respectively in Tauber et al. (2010). The primary spillover originates mainly from directions on the sky close to the spin axis. This is hence expected to be roughly constant for each fixed pointing period, and will be removed by our destriping procedure. The baffle spillover corresponds to radiation reaching the detectors after reflection on the environment, including the telescope's baffles. Again, one may expect this component to be roughly constant over a ring, as a result of the averaging of a lot of original directions. Finally, the secondary spillover is picked through a wide ($\sim 15^\circ \times 30^\circ$) area $\sim 10^\circ$ aside from the main beam (see Fig. 5 in Tauber et al. (2010)) and is built by radiation reaching the HFI horns without reflection on any telescope part. This will gather an image of the sky offset with respect to the main beam and integrated over a very broad beam. In particular, it will contain a dipole component.

Table 2 in Tauber et al. (2010) gives the relative amplitudes of the different FSL components with respect to the main beam signal, combining secondary and baffle spillovers in the 'SR' column. One may see that, in this framework, PR and SR have comparable amplitudes. At maximum, the SR relative amplitude amounts to 0.2% at 100 GHz and decreases fast for frequencies larger that 217 GHz. To clarify the baffle spillovers importance, we performed simulations with the actual *Planck* scanning strategy and FSL models similar to those of Tauber et al. (2010). This indicated that the SR FSL signal after destriping had an amplitude of $\sim 70\%$ of Tauber et al. (2010)'s Table 2. This is confirmed by the estimations of the FSL amplitudes presented in Planck Collaboration XIV (2013), which gives confidence in the models used in Tauber et al. (2010). From this, as shown in Planck Collaboration VII (2013), we conclude that, at maximum, a spurious dipolar signal with a relative amplitude of $\sim 0.13\%$ could be present in our data. As the CMB is a Gaussian signal, neglecting the beam transfer function i.e., at very low ℓ ($\ell \leq 30$ given the SR beam), one may then consider that

$$S_{FSL} = \varepsilon_{SR} S_{ML} + constant \quad (5)$$

at ring level. Thus our calibration will determine an effective gain: $g_{eff} = g(1 + \varepsilon_{SR})$. This will lead to reconstructed sky signal approximately equal to S_{ML}. Therefore, at large angular scales, ignoring in the calibration process the spurious SR signal remaining after destriping, cancels at first order the effect of not accounting for it in further analysis (like power spectra). At smaller scales however, the SR signal becomes negligible and this cancellation is not effective anymore. To conclude, the HFI dipole calibration as done for the 2013 data release may result in a $\sim 0.25\%$ overestimate of the band powers for ℓ above ~ 40. This $\sim 0.13\%$ calibration systematics is lower than other sources of systematic uncertainties evaluated later in this paper.

3. Pipeline for map production

The products of the HFI mapmaking pipelines are pixelized maps of I, Q and U together with their covariances, based on the HEALPix scheme (Górski et al. 2005). For a given channel, data sample number i may be described as :

$$d_i = G\left(I_p + \frac{1-\eta}{1+\eta}\left(Q_p \cos 2\psi_i + U_p \sin 2\psi_i\right)\right) + n_i \quad (6)$$

where p denotes the sky pixel with Stokes parameters I_p, Q_p and U_p, n_i is the noise realization, η is the cross-polarization parameter (equal to 1 for an ideal spider web bolometer and 0 for an ideal polarisation sensitive bolometer), ψ_i is the detector orientation on the sky, at sample i, and G is the detector's gain. Given *Planck*'s scanning strategy, reconstructing I, Q and U requires to combine measurements from several detectors for most pixels. According to bolometer models, G is expected not to vary significantly, given the stability of the HFI operational conditions during the mission.

In order to deal more efficiently with the large HFI data set and the number of maps to be produced, we use a two step scheme to make maps from the HFI TOIs. The first step takes advantage of the redundancy of the observations on the sky. For each detector, we average the measurements in each HEALPix pixel visited during a stable pointing period (hereafter called *ring*). The subsequent calibration and mapmaking operations use this intermediate product, called HPR for *HEALPix Pixels Ring*, as input. As we produce HEALPix maps with the resolution parameter $N_{\rm side}$ set to 2048 we use the same internal resolution for building the HPR.

The in-flight noise of the HFI detectors, after TOI processing, is mostly white at high frequency, with a '1/f' increase at low frequency (Planck HFI Core Team 2011a). In such a case, a destriping approach is well adapted for the mapmaking (Ashdown et al. 2009). In this approach, the noise in a ring r is represented by an offset, noted $\mathbf{o_r}$, and a white noise part $\mathbf{n}$, which is uncorrelated with the low-frequency noise. We may then reformulate Eq. 6 as:

$$\mathbf{d_i} = G \times \mathbf{A_{ip}} \cdot \mathbf{T_p} + \mathbf{\Gamma_{ir}} \cdot \mathbf{o_r} + \mathbf{n_i}, \quad (7)$$

where $\mathbf{T}$ represents the sky (which may be a 3-vector if polarization is accounted for) in pixel p, $\mathbf{A}$ is the pointing matrix (which makes the link between data samples and their positions on the sky) and $\mathbf{\Gamma}$ is the matrix folding the ring onto samples. From the above equation, $\mathbf{o_r}$ are derived through maximum likelihood. As there is a degeneracy between the average of the offsets and the zero level of the maps, we impose the constraint $\langle o \rangle = 0$. We have shown (Tristram et al. 2011), that with a scanning and noise such as those of HFI, an accurate reconstruction of the offsets $\mathbf{o_r}$ requires a precise measurement of G for each channel.

In addition, some signal components vary with time, adding some complexity to Eq. 7. Such components are the zodiacal light emission, the CMB dipole anisotropy component induced by the motion of the satellite with respect to the Solar System and the FSL pick-up signal. Time variability of the former comes from the variation of the observation angle of the Solar System region emitting this radiation due to the ellipticity and cycloid modulation of the satellite's orbit. Accounting for these components in the mapmaking process requires an accurate calibration. On the other hand, we need to take into account the low frequency noise within the calibration, so both operations are interleaved.

For the production of the maps of the 2013 HFI data release, we followed a four-step process:

1. We first build the HPR for all detectors, for three datasets: all the data for each ring and only the first (resp. second) half of each ring to enable null tests.
2. From these HPR we then perform the different calibration operations, namely:
   - the Solar dipole calibration, which sets the overall calibration factor for 100 to 353 GHz detectors,
   - the planets calibration (Uranus and Neptune), which is used to get the calibration factor for 545 and 857 GHz detectors,
   - and the `bogopix` tool (see Sect. 4.3) is then used to determine the relative gain variations of 100 to 217 GHz detectors.
3. Finally, we proceed for each dataset to the destriping and projections. We use the `polkapix` tool that is thoroughly validated in Tristram et al. (2011). We compute one set of offsets using the whole mission dataset, and then use these offsets to compute the maps, for the whole mission as well as for restricted time intervals (corresponding to each individual survey, and to the nominal mission). Maps are built by simple co-addition in each pixel of the destriped, calibrated and time varying component subtracted signal. We subtract the *WMAP* measured CMB dipole, using the classical approximation, from all our maps. We produce all maps with a HEALPix resolution parameter $N_{\rm side} = 2048$.
4. The zero-level for the maps are set, in this release, a posteriori, because of the late revision of the high frequency calibration method.

We produce single detector temperature maps as well as temperature and polarization maps using all detectors of a single frequency and detector subsets, enabling various null tests. We also produce hit count maps as well as variances maps for the I, Q and U values computed in each pixel. Overall, a grand total of $\sim$ 6500 sky maps has been produced. We used this dataset to evaluate the performance of the photometric calibration in the following. Note that the HFI pipeline we have described is quite similar to what is done for LFI (Planck Collaboration II 2013).

In order to take into account the far side lobe (FSL) and zodiacal light (hereafter called `zodi`) components, which vary in time, we have constructed templates for the combination of these components at frequencies where FSL matters, 545 and 857 GHz, and of `zodi` only at lower frequencies, as described in Planck Collaboration XIV (2013). These templates are used to build HPR that are systematically subtracted from the data of each detector prior to the mapmaking. We provide two sets of maps. The first one is built without removing these spurious components. The second one gives the correction obtained when subtracting them and might be used to correct the HFI maps for specific cases.

We will describe in the following sections the calibration procedures before assessing their performances, and give some characteristics of the resulting maps.

4. Photometric calibration of the low-frequency channels: dipole-based calibration

4.1. Solar dipole calibration

For the HFI data from bolometers observing at frequencies below and including 353 GHz, the photometric calibration is performed using the CMB dipole.

We estimate one value of the detector gain for each ring through a template fit of the HPR data. We fit a model of linear combination of dipole, Galactic signal and noise, neglecting the CMB and the polarization. For each ring, the fitted model reads:

$$\mathbf{d} = g_r^D.\mathbf{t}_D + g_r^G.\mathbf{t}_G + c_r + \mathbf{n} \quad (8)$$

where $\mathbf{d}$ represents the HPR samples from ring r, $\mathbf{t}_D$ is the value of the total (Solar and orbital) kinematic dipole, $\mathbf{t}_G$ is a model for the Galactic emission and $\mathbf{n}$ is the white component of the noise. We fit simultaneously three parameters:

- g_r^D the gain on the kinematic dipole,
- g_r^G the gain on the Galactic model,
- c_r, a constant, which enables to account for the low frequency noise.

As the satellite scans circles on the sky, the ratio of the dipole and Galactic signal amplitudes varies. We use a Galactic model to get a measurement of the dipole gain even in rings where the dipole amplitude is low. However, imperfection of that model may lead to bias in the dipole gain. To reduce the bias, we excluded pixels with a Galactic latitude lower than 9°. As we calibrate on the kinematic dipole, we will not use the gain g_r^D in the following. Pixels contaminated by point sources from the Planck Catalog of Compact Sources catalog (Planck Collaboration XXVIII 2013) are also excluded. The best model we have for the sky emissions at the HFI frequencies being HFI measurements themselves, we use HFI sky maps as a Galactic model.

Results of the gain estimation for each ring is shown for one detector (143-3a) on Fig. 1. Due to the *Planck* scanning strategy, gain estimation is less accurate on some ring intervals corresponding to when *Planck* spin axis is orthogonal to the dipole direction. The final gain value for each detector, hereafter noted $\tilde{G}^d$, is defined as the average of the estimations between rings 2000 and 6000, were the individual measurements for each ring are dispersed by less than 1 %.

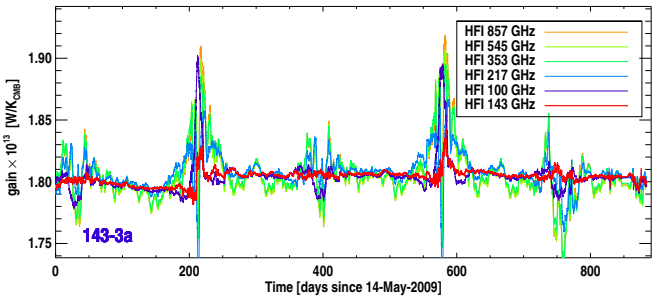

Figure 1. Impact of the Galactic template on the Solar dipole ring gain measurements. We compare the results obtained using the HFI temperature maps at each frequency (from e.g., previous reconstructions). For this plot, ring by ring gains have been smoothed with a smoothing width of 50 rings (which corresponds to ∼ 2 days). Rings for which the Solar dipole's amplitude is low with respect to Galactic emissions are those where larger variations occur (around days 50 , 200, 400, 550 and 700). Using the HFI map at the detector's frequency as a Galactic template minimizes the systematic ring-to-ring variations.

We evaluate the impact of the choice of a Galactic template on Fig. 1. We compare the ring by ring gains obtained using the different HFI frequency maps. Using a Galactic template helps recovering an estimation of the calibration factor for rings scanning regions close to the Galactic equator (e.g around day 200). Unsurprisingly, the template producing the lower apparent variations is that of the same frequency as that of the studied detector. However, even in this case, in the time interval where the dipole amplitude is low, apparent systematic gain variations are observed. In Fig. 2 we show results obtained when taking in addition into account the polarization (from the HFI Q and U maps). The small difference this induces shows that polarization does not play a major role in the apparent ring-to-ring variations, even for rings where Galactic emissions are larger.

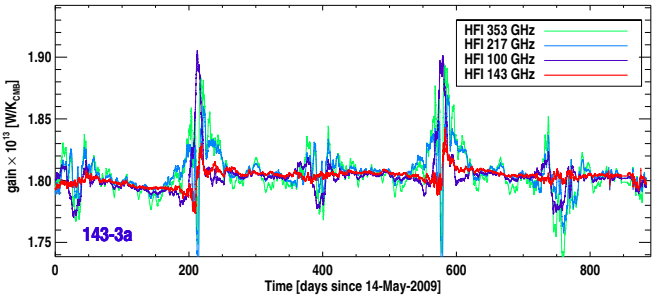

Figure 2. Same plots as Fig. 1, but taking into account polarization as reconstructed in the HFI Q and U maps. This induces very little differences with respects to results shown of Fig .1, which shows that polarization is not the main source of systematic variations for the rings where Galactic emissions are larger.

We observe apparent ring-by-ring gain variations, of the order of ∼ ±1 %. To assess the reality of such variations, we compared the ring-by-ring apparent gain variations reconstructed in survey 1 and 3 (and 2 and 4 respectively). An example of such comparison is presented in Fig. 3. Rings from surveys 1 and 3 (resp. 2 and 4) followed parallel trajectories on the sky, separated by ∼ 1.′25. Given the HFI beams typical full width at half maximum (FWHM), any sky induced systematics should therefore be very similar in both cases. As can be seen in Fig. 3, we indeed find that the gain difference between survey 2 and 4 is clearly visible. In addition, fast (over ∼ 10 rings) variations of the gain seem to show up e.g., in the second part of survey 3 or at the beginning of survey 4.

This indication of apparent gain variation is supported by studying the difference between maps restricted to survey 1 and 3 (resp. 2 and 4), which is illustrated in Fig. 4. As stated above, the path followed on the sky during survey 1 and 3 (resp. 2 and 4) are nearly identical, so in the difference of the maps from these surveys, sky signal and sky induced systematics should cancel out. These differences are therefore principally sensitive to instrumental effects like pointing accuracy, time response deconvolution and calibration stability. Indeed, in the differences shown in Fig. 4, we observe large scale residuals with characteristic dipole structure, along the scan direction, which trace the apparent gain variations observed in Fig 3.

We conclude that the HFI bolometers sensitivities seem to present an apparent response variation with time, of ∼ 1 − 2 %. The time scales of these variations ranged from days to months. One should note that the existence of time variation in detector response breaks one of the fundamental assumptions of our planned orbital dipole absolute calibration scheme.

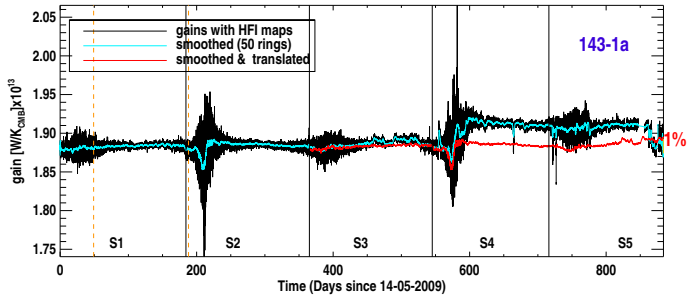

Figure 3. Solar dipole gain reconstructed ring by ring for one HFI bolometer. The thin black line represent the raw values, the thick cyan lines are smoothed rendition with a 50 rings (~ 2 days) width. We indicated the conventional limits of the surveys as black vertical lines. The orange vertical dotted lines indicate the interval in which we compute the gain G_d^*. We finally indicate in red the smoothed gain variation shifted to match the repetition in surveys 3 and 4 of the scan strategy followed in surveys 1 and 2. Note however that the scan strategy for survey 5 differs from that of survey 3.

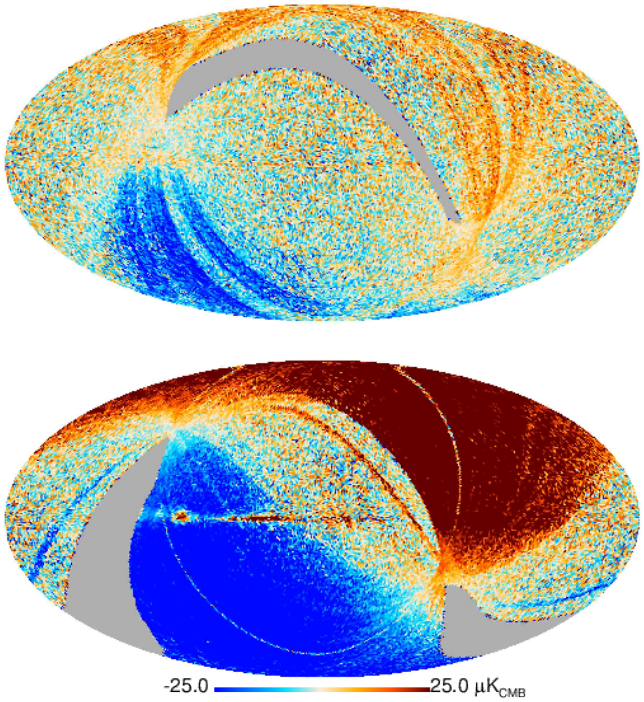

Figure 4. Differences between temperature maps built using data from detector 143-1a, for surveys 1 and 3 (top) and 2 and 4 (bottom). In both cases, large scale features appear. Their amplitude and disposition on the sky are compatible with residuals from the Solar dipole, due to time variations of the detector gain, of the order of 1 to 2 % These residuals should be compared to the amplitude of the Solar dipole, 3.353 mK$_{CMB}$.

4.2. Study of the apparent gain variations

Comparing survey 3 and survey 1 data made the existence of time variations of the measured bolometers responses indisputable. Intrinsic bolometer sensitivity variations cannot explain such observations. The HFI bolometers have been precisely characterized in flight using dedicated $V(I)$ sequence of measurements, during the post-launch verification phase and end-of-life periods. The static bolometer models predicts that changes of their background during the observations could not explain response variations larger than 0.1 %. In addition, such variations are corrected for within the HFI DPC pipeline. In our present understanding, these apparent response variations are the result of imperfections in the linearity of the analog-to-digital converters (ADC) used in the bolometers read-out units. The variation of the bolometer background with time and the inequality of the ADC quantization steps leads at first order to an apparent electronic chain gain variation. These non-linearities may also affect signal differently depending on their amplitude (for example the Solar and orbital dipoles).

Ground measurements on spare ADC have been conducted. Figure 5 shows the error on the transition code positions measured on one chip around the ADC mid scale, which is the most populated area. This so-called Integrated Non-Linearities (INL) present a prominent feature for all the channels: the central step is always too narrow. In addition to this, the 64-code nearly periodic patterns also play an important part in building the apparent gain variations, making a prediction of the consequence of such errors on the reconstructed, demodulated, bolometer signal very complex. Such an INL effect has been input in full mission simulations and reproduces well the gain variation features observed in real flight data.

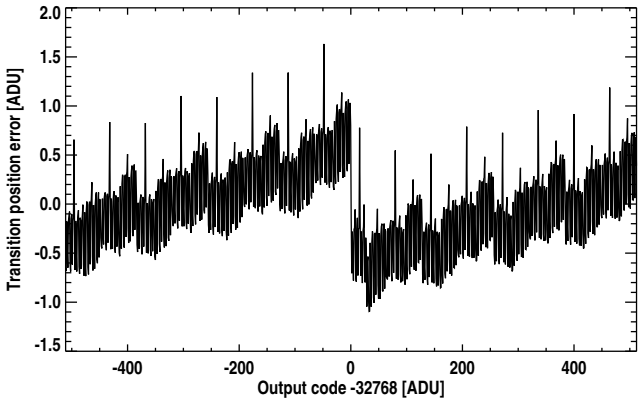

Figure 5. Error on transition code positions measured on one chip around the ADC mid scale, on ground on a spare ADC. The largest error occurs at the sign transition, but ~ 1 ADU error also regularly occur every 64 bits.

In order to be able to precisely correct for this effect for all data samples, we need accurate measurements of all ADC INLs together with a good model for the bolometer raw signal (including systematics). Mapping the ADC response was found to require more data than were at hand at the end of the HFI cold life-time, and a dedicated campaign is being conducted for several months, with a focal plane temperature of about 4K, giving a clean ADC characterization on Gaussian noise. At the time of writing, correction procedures are being intensively tested on a few detectors. Correcting this effect needs to be done prior to the TOI processing steps of the HFI data reduction and requires thorough checks of any ulterior intermediate products.

4.3. Effective correction and characterization

In order to be able to handle time variation of the bolometer gains, we set-up an effective correction tool, hereafter named

bogopix (Perdereau 2006). We start from equation 7, but take explicitly into account the orbital dipole $\mathbf{t}_{Do}$, which is time variable and also fit the gains $\mathbf{g_r}$ for each bolometer independently. The problem finally reads

$$\mathbf{d} = \mathbf{g_r}(\mathbf{A}\cdot\mathbf{T} + \mathbf{t}_{Do}) + \mathbf{\Gamma}\cdot\mathbf{o_r} + \mathbf{n}, \quad (9)$$

where r the ring number. The unknowns are the offsets $\mathbf{o_r}$, the sky signal represented by $\mathbf{T}$, as previously, and the gains $\mathbf{g_r}$, sampled using one value per ring. Since the orbital dipole is an absolute calibrator, the solution for $\mathbf{g_r}$ should also fix the absolute photometric calibration.

We take advantage of the low amplitude of the observed gain variations to linearise this nonlinear problem, following an iterative approach. Starting from a approximate solution for the gains $\mathbf{g_r}$ and sky maps $\mathbf{T}$, we determine variations with respect to these, respectively $\delta\mathbf{g_r}$ and $\delta\mathbf{T}$, by solving :

$$\mathbf{d} = (\mathbf{g_r} + \delta\mathbf{g_r})(\mathbf{A}\cdot(\mathbf{T} + \delta\mathbf{T}) + \mathbf{t}_{Do}) + \mathbf{\Gamma}\cdot\mathbf{o_r} + \mathbf{n} \quad (10)$$

$$\approx \mathbf{g_r}(\mathbf{A}\cdot(\mathbf{T} + \delta\mathbf{T}) + \mathbf{t}_{Do}) + \delta\mathbf{g_r}(\mathbf{A}\cdot\mathbf{T} + \mathbf{t}_{Do}) + \mathbf{\Gamma}\cdot\mathbf{o_r} + \mathbf{n} \quad (11)$$

The linearized Eq. 11 may then be solved through conjugate gradient (CG) for $\delta\mathbf{g_r}$, $\delta\mathbf{T}$ and $\mathbf{o_r}$. Using $\delta\mathbf{g_r}$ and $\delta\mathbf{T}$ the gains $\mathbf{g_r}$ and sky maps $\mathbf{T}$ can finally be updated. This process is iterated until a satisfactory solution is reached. To initialize the iterations, we start from the constant gain solution. We stop the iterations when the variation of the χ^2 derived from Eq. 9 is low enough. However, tests showed that this simultaneous fit of sky signal and gains is not well conditioned, at least with a scanning strategy similar to that of *Planck*. This approach is similar to what is being used in the Low Frequency Instrument (LFI) calibration (Planck Collaboration V 2013). It was successfully tested with the dataset used in Tristram et al. (2011). In this work, we built simulated timelines with a *Planck*-like scanning strategy, realistic noise (both for the white and 1/f components), gaussian beams and single frequency bandpass, for four 143 GHz PSBs over ∼ 12000 rings. Figure 6 presents gains reconstructed with bogopix on simulated data, and compares them with the constant input gain values. From these results, we see that the precision on the gain value reconstructed for a single ring is ∼ 0.5 % (which is on par with the global precision of ∼ 5×10^{-5} for a constant gain for ∼ 12000 rings found in Tristram et al. (2011)).

We computed the gain variations using single detector data, thus neglecting polarization. To avoid any bias, we ignore sky regions where the polarized emission is larger, and which lie mostly in the Galactic plane. As for destriping (Tristram et al. 2011), gradients inside the sky pixels used for $\mathbf{T}$ will also limit the accuracy of the gain determination. These gradients increase with frequency. Moreover, the ADC non-linearity will induce larger biases in the signal used for the gain determination for higher frequencies, which spans a wider range. For these reasons, we used bogopix to determine an effective correction for the apparent gain variations only for frequencies lower than or equal to 217 GHz.

As shown in Fig. 7, the variations we find with bogopix follow nicely those of the Solar dipole calibration in the regions where this signal is large. The lower level of fast variations of bogopix results in the time intervals where the scan lies close to the solar dipole equator and in the same time close to the Galactic plane, indicates that bogopix results are less biased for these rings. We observe apparent gain variations on time scales of few hours as well as months, with amplitudes of 1 to 2 % maximum, largely uncorrelated from one detector to the other.

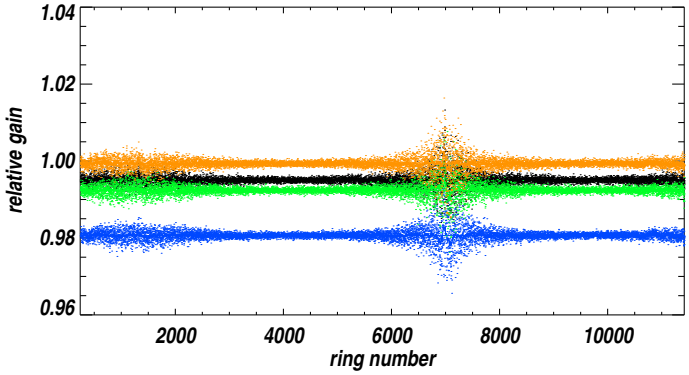

Figure 6. Example of results obtained with bogopix on the simulated dataset used in Tristram et al. (2011), with constant input gains. Each color represent the results for a given bolometer. Dots correspond to individual measurements, and the thick line is a smoothed representation of these results with a 50 rings width.

The averaged sensitivity determined by both methods seem however to be different, and this difference, typically of 0.5 to 1 %, varies from one detector to another. We believe this is due to the different scales of the calibrating signals in both methods: the absolute scale of bogopix results is set by that of the orbital dipole, a factor of 5 to 10 lower in amplitude that the Solar dipole used in the other method. These signals are thus affected in different proportions by the ADC non-linearities, which explains the difference between the averaged gains reconstructed by both methods. Indeed, in the simplest case, the effect of the ADC digitization steps non-uniformity can be seen as a fixed offset (positive or negative) added on top of the signal, when this signal oversteps a given level. Therefore, the resulting calibration bias will be lower for the largest calibration signal. In order to understand this difference, we used the orbital dipole calibration tool described in Tristram et al. (2011), together with bogopix gains, renormalized so that they average to 1 between rings 2000 and 6000 (corresponfing to days 60 and 190 approximately), to correct for the apparent gain variations. The relative difference between the orbital dipole and solar dipole gains are shown in Fig. 8, where they are also compared with the relative difference between the average of the bogopix gains and the solar dipole gain. Both methods agree with each other within 0.05 to 0.1 %. We showed in Tristram et al. (2011) that calibration errors induce large scale features in the Q and U Stokes parameters maps. When using the orbital dipole based calibration factors to build these maps, we indeed observe such large scale patterns, which is another evidence that the latter factors are biased. We also observed a noticeable residual dipole in the reconstructed detector maps, for those where the difference between the Solar and orbital dipole calibration was larger, after subtraction of the WMAP measured dipole. We therefore concluded that, in the absence of an accurate correction for the ADC non-linearities, the orbital dipole calibration scheme cannot be used to calibrate HFI data.

4.4. Dipole calibration pipeline

As a conclusion, we used bogopix results only as a measurement of the *relative* gain variations, by normalizing to 1 on average between rings 2000 and 6000 (where the Solar

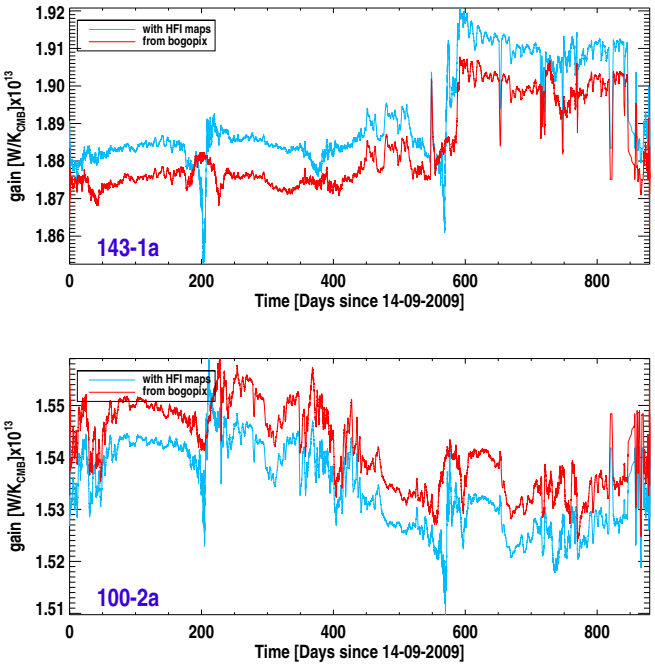

Figure 7. Example of results from `bogopix` obtained for two HFI detectors, compared with those of the Solar dipole calibration. Gain values for individual rings have been smoothed with a width of 50 rings (~ 2 days), to increase the signal-to-noise ratio of the plots. We observe a good agreement between `bogopix` results and those obtained with the HFI maps, for the relative gain variation, except for the time intervals where the Solar dipole's amplitude is low with respect to the Galactic emission. The averaged value of the gains are, however, offset by factors (different from one detector to the other) of the order of 0.5 to 1 %.

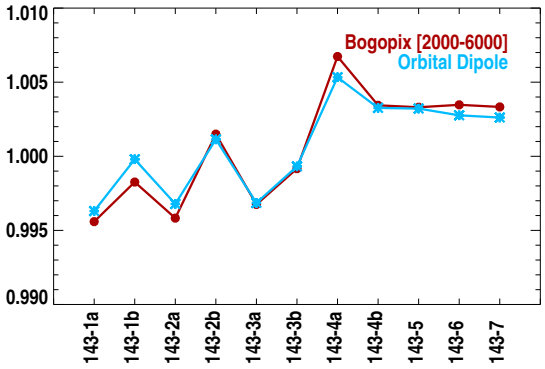

Figure 8. Photometric gain relative differences w.r.t the Solar dipole calibration results, for the orbital dipole calibration (orange) and the average of `bogopix` gains (red), for the 143 GHz HFI detectors. Both schemes produce gains within 0.1 % of each other, which shows they are both affected by the same systematics, the ADC non-linearities.

dipole calibration is computed). We show for example on Fig. 9 a compilation of the relative gains reconstructed for the 100, 143 and 217 GHz detectors. The absolute calibration scale of the HFI CMB channels (100-353 GHz) is set by the Solar dipole calibration, as for the HFI early data release (Planck HFI Core Team 2011a), which relies on *WMAP* Solar dipole measurements (Hinshaw et al. 2009).

As a first example of the improvements that `bogopix` provides, we show on Fig. 10 the residual differences between maps restricted to survey 1 and 3 (resp. 2 and 4), for the same detector used for Fig. 4. The differences obtained using `bogopix` are lower than $\sim 10\,\mu K_{CMB}$ outside the Galactic plane. Residual still present, in particular in the survey3-survey1 difference, in that region may be interpreted as the consequence of the nonlinear nature of the systematic effect, of which only the first order linear part is handled by `bogopix`.

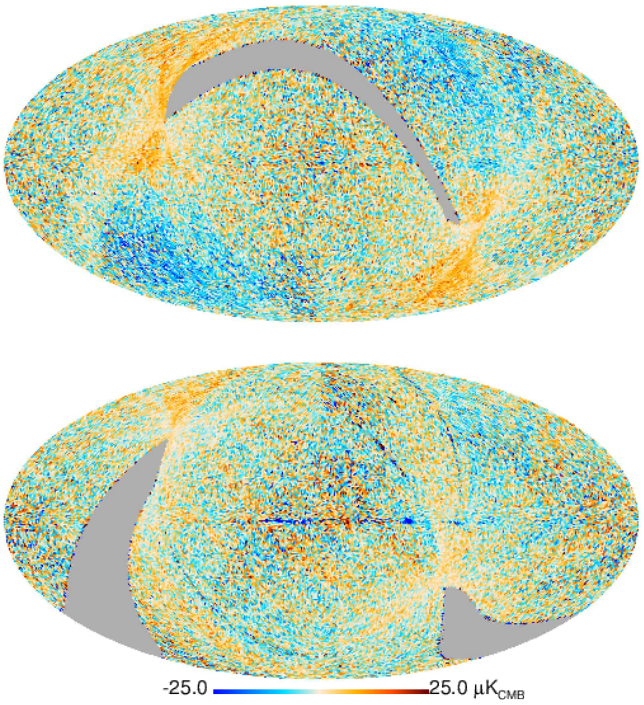

Figure 10. Residual differences between temperature maps built using data from detector 143-1a, for surveys 1 and 3 (top) and 2 and 4 (bottom), obtained when applying the `bogopix` results. The level of such differences is much lower than what is shown on Fig. 4.

For frequencies higher or equal than 353 GHz, `bogopix` results are not reliable mainly because of too large spatial variation of the sky emissions inside a pixel (we have used 1.72′). Therefore, we do not correct the highest frequency channels for any gain variations. This leads to ~ 1 % calibration uncertainties between maps of individual surveys.

4.5. Dipole calibration uncertainties for single detector

For the dipole calibration scheme, the statistical uncertainties are estimated by propagating the TOI sample variances (NET) to the ring-by-ring gains estimation on the Solar dipole, averaged between rings 2000 and 6000, for each detectors. These uncertainties are much lower than the systematic uncertainties that dominate our calibration measurement. We estimate these systematic uncertainties on calibration of individual detectors by measuring the dispersion of these ring-by-ring gains. Both uncertainties are listed in Table 2, which gives their average at each frequency. The *WMAP* Solar dipole amplitude uncertainty (0.24 %, Hinshaw et al. (2009)) is not included. The systematic

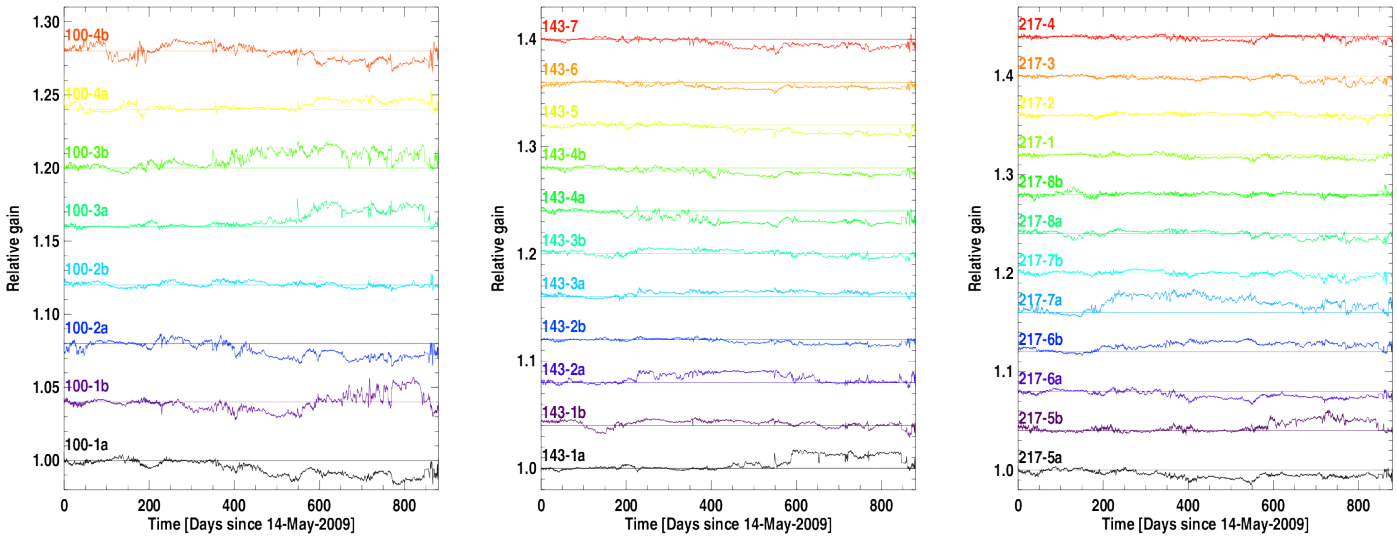

Figure 9. Relative gains reconstructed by `bogopix` for the 100, 143 and 217 GHz detectors as a function of time, smoothed with a width of 50 tings (~ 2 days). Their overall amplitudes are of order 1 to 2 % but slow as well as fast (over a few tens of rings i.e., a day) variations are observed. These variations are largely independent from one detector to therr other. Relative gains for each detector have been vertically displaced by 3 % for readability.

Table 2. Statistical and systematic uncertainties on the dipole calibration, for single detectors from the HFI lowest frequency channels. The "worst case" column corresponds to a situation with an ill-adapted sky template, whereas the third column is for the best case. In addition to each of these values, one has to take into account the *WMAP* Solar dipole amplitude uncertainty, 0.24%, as this measurement is our primary calibrator.

Frequency [GHz]	Statistical error [%]	Systematic (worst case) [%]	Systematic [%]
100	0.004	0.64	0.37
143	0.002	0.53	0.29
217	0.002	0.69	0.41
353	0.01	2.53	1.81

errors given here should be considered as upper limits of the real systematics, as they have been derived from Solar dipole ring by ring gains prior to the `bogopix` correction. We indicate the effect of the choice of template by indicating a 'worst case' scenario (second column of the table) in which a non optimal template was used. When combining detectors with each other, some of these systematic errors should partially average out for temperature. The gain variation part for example is independent from one to the other. To get a more precise estimation of the calibration accuracy for the frequency maps of this release, we have performed more elaborate tests presented in Sect. 7.

5. High-frequency channels photometric calibration

5.1. From a FIRAS- to a planet-based absolute calibration

Since the early times of the *Planck* data, it has been noticed that the ratio between HFI and FIRAS is not constant across the sky: we observe spatial gain variation (i.e., variation of K, and thus variation of O, see Eq. A.3), that mimics a decrease of the calibration coefficient K with brightness[3]. Comparison with the dipole calibration at 353 GHz showed that the high latitude gradients ($10° < |b| < 60°$) gave a better agreement. It was thus adopted for the calibration of the *Planck* early results papers (*Planck* Early Results. VI. The High Frequency Data processing).

We investigated again this unresolved discrepancy with the FIRAS maps, in the preparation of the first major release. As detailed in Appendix A, numerous tests and checks have been conducted. However, we could not find any remaining HFI systematics, nor a bias in our method of comparison of the two datasets, that could explain such a discrepancy. The only alternative comes from a systematic bias in the FIRAS pass4 interstellar dust spectra. Indeed, Liang et al. (2012) propose a new set of FIRAS dust spectra that leads to a significant revision of the dust spectra, in the right direction compared to the discrepancy observed with HFI (see their Fig. 1).

In parallel, converging evidences of an overestimate of the HFI brightness at high frequencies, when calibrating using FIRAS, came to light (see Sect. A.5). These evidences lead us to propose a change in the photometric calibration scheme for the sub-millimetre channels. We are now using the planet flux measurements. The ultimate scheme would be to intercalibrate the 545 and 857 GHz channels with the CMB channels, using the planets models as a relative calibrator. Indeed, for the Neptune and Uranus planet models used for the calibration, the scale of the model is known to about 5 %, whereas the relative inter-frequency uncertainty is expected to be of order of 2 % (Moreno 2010). We present hereafter our calibration procedure for the high-frequency channels of the 2013 data release.

[3] these should not be mixed up with the apparent gain variation with time discussed in Sect. 4.2

5.2. Planet flux densities: measurements and comparison with the models

Planck observes the five outer planets: Mars, Jupiter, Saturn, Uranus, and Neptune. The 21 planet observations made by *Planck*-HFI have been analysed. For calibration purpose, only Neptune and Uranus are used as (i) Jupiter is in part in the non-linear regime, (ii) Jupiter and Saturn have strong absorption features that make the comparison with the broad-band measurements difficult, (iii) Mars flux is strongly varying from season to season. Even if this can be handled precisely by the models, this complicate the analysis, so that we defer the use of Mars to the future release. For the present data release we applied correction factors to the FIRAS-based calibration coefficients to match the Uranus and Neptune flux densities given from the Moreno (2010) model.

5.2.1. HFI beams and solid angles

The HFI beam solid angles used in this analysis are those derived from Mars observations. We do not use solid angles from the beams that are averaged over the scanning history (the so-called *effective* beams (Planck Collaboration VII 2013)), because we consider each observation of Uranus and Neptune for each bolometer separately, and therefore we do not need to compute an average point spread function. We correct for the small response at large scales (beyond 40′ from the beam centroid) due to incomplete deconvolution of the bolometer/readout electronics time response as measured on Jupiter. Details on the beam solid angle measurements are given in Planck Collaboration VII (2013).

The measured beam solid angle depends on the SED of the source. The solid angle for a planet (with an SED roughly in ν^2) is different from that for the photometric convention νI_ν = cst. Maffei et al. (2010) and Tauber et al. (2010) investigated the variation of the beam size across the planet using a pre-launch telescope model. For the lowest frequency HFI bands 100, 143, and 217 GHz, the beam size reaches a minimum near the center of the band making the solid angle a weak function of source SED. The beam colour corrections for these bands are expected to be less than 0.3 %. At 353 GHz the solid angle increases with frequency across the band, but the beam colour corrections are expected to be less than 1 %. The multi-moded horns at 545 and 857 GHz are more difficult to model because of uncertainty in the relative phase and amplitudes of the modes propagating through each horn. The models of Murphy et al. (2010) give an upper limit in the beam colour correction to the solid angles of 2 % and 1 % at 545 and 857 GHz respectively.

The FWHM of the beams on the sky is defined by the energy distribution at the entrance of the horns, which - due to the optical design of the Planck telescope - does not depend much on the frequency within the spectral band. The throat of the horns are positioned very close to the focal plane of the telescope, with a deviation varying from horn to horn. If the deviation is small, the variation of the beam solid angle on the sky will be symmetric around the centre of the band, and the combined correction will be small. If the horn is significantly offset, the variation will not be symmetric, and the correction will be larger. An estimate of the correction is described in Planck Collaboration VII (2013).

Note that this nearly null variation of the solid angle inside the band is unusual for sub-millimeter experiments. For example for SPIRE on Herschel, the FWHM varies by ±17% across the passband. The SPIRE beam solid angles have been measured on Neptune; using the photometric convention νI_ν = cst, the corrections to the beam solid angles are about 3.3 and 5.9% at 350 and 500 μm, respectively (Griffin & al. 2013) For HFI, as seen above, the corrections are much smaller, and for now the beam solid angle variation for the high-frequency channels has not been taken into account in the calibration. Its effect is negligible compared to the error we have on the photometry (see the next section).

5.2.2. Uranus and Neptune flux measurements and model comparison

Our calibration procedure followed the following steps:

- A first photometric calibration was set using FIRAS at 545 and 857 GHz.
- We created 2°×2° maps with a 2′ pixel size around the planets position by projecting the destriped and calibrated timelines, using the nearest grid point algorithm, from timelines scanning each planet.
- We simultaneously built maps of the same sky area, using observations taken at different epochs (when the planet was at a different position) to estimate the sky background, and subsequently subtract it from the planets maps. At $\nu \leq$ 353 GHz, the background is so small that removing it has a negligible impact. At 857 GHz, the astrophysical background starts to become a few percent of the peak signal of Neptune.
- We measured the planet flux densities using aperture photometry on maps. We integrated the flux up to 3×FWHM in the background-subtracted maps. We corrected for the beam solid angle difference between 3×FWHM and the full solid angle. This correction amounts to 0.8 % at 545 GHz and 1.5 % at 857 GHz.
- At 545 and 857 GHz, we applied a correction factor to the FIRAS calibration to match the Uranus and Neptune flux densities given by the models. The factors were the same for all bolometers inside a frequency, namely 1.07 at 857 GHz, and 1.15 at 545 GHz.

The measurements are color corrected (using Eqs. 1 and 2) and the flux densities are quoted for the two planet spectra. Color corrections vary from about 0.92 (353 GHz) to 1.05 (143 GHz). In the sub-millimeter channels they are <2 % at 857 GHz and ~5 % at 545 GHz. Errors on the color corrections are detailed in Planck Collaboration IX (2013), and are estimated as 0.25, 0.06, 0.01, 0.006, 0.003, 0.002 % from 100 to 857 GHz.

From the flux densities and the planet solid angles estimated for HFI at the date of the observations, we can compute the brightness temperatures T_B. They are given in Table 3, where we averaged the flux densities computed for all detectors in a channel, and all observational seasons (four), prior to the computation of T_B. The quoted error on T_B comes from the standard deviation of the flux measurements.

We use the models called ESA2 for Uranus and ESA3 for Neptune developed by R. Moreno (Moreno 2010) for the *Herschel*-SPIRE absolute photometric calibration. The millimetre and sub-millimetre spectrum of Uranus and Neptune was modeled with a line-by-line radiative transfer code accounting for the spherical geometry of their planetary atmospheres as that described for Titan by Moreno et al. (2011). Atmospheric opacity due to minor species CO (for Neptune only), NH_3 far wings, and also collision-induced opacities of the main species

Table 3. Neptune and Uranus brightness temperatures measured by HFI. At high-frequencies, the numbers are not independent measurements of the planet flux densities, as the 545 and 857 GHz channels have been *re-calibrated* to match simultaneously the Uranus and Neptune flux densities given by the models.

Frequencies [GHz]	Uranus T_B [K]	Neptune T_B [K]
100	124.3±5.0	129±15
143	108.4±2.9	110±6
217	97.0±2.5	96.9±3.7
353	83.3±2.3	81.1±2.7
545	(73.7±2.4)	(71.2±2.1)
857	(67.5±1.3)	(65.0±1.9)

(H_2, He, CH_4) were included. The thermal profiles were taken from Lindal (1992) in the troposphere, which is the atmospheric region probed between 90–900 GHz. The uncertainty of the computed brightness temperature is mainly linked to the uncertainty on the thermal profile with an absolute uncertainty value of 5 %. The relative calibration (between frequencies) is expected to be at the order of 2 %.

We compute the flux densities using the brightness temperatures from the model and the planet solid angles estimated for HFI at the date of the observations. The model spectra (in Jy) are interpolated onto our bandpass frequencies, and convolved by our bandpass filters to get the flux densities as measured by HFI. We show on Fig. 5.2.2 the comparison of the flux measurements with the models. Error bars on the HFI data points correspond to the standard deviation of the measurements (all bolometers, all seasons). For the two high frequencies (857 and 545 GHz), the agreement with the model has been forced by our calibration procedure. For the lower frequencies, calibrated using the dipole, we have an overall very good agreement with the model, the two being compatible within the error bars. Fig. 12 shows the same comparison but on spectra in brightness temperature, and with other measurements from the literature. Notice the very good accuracy of the HFI measurements on a large range of frequencies.

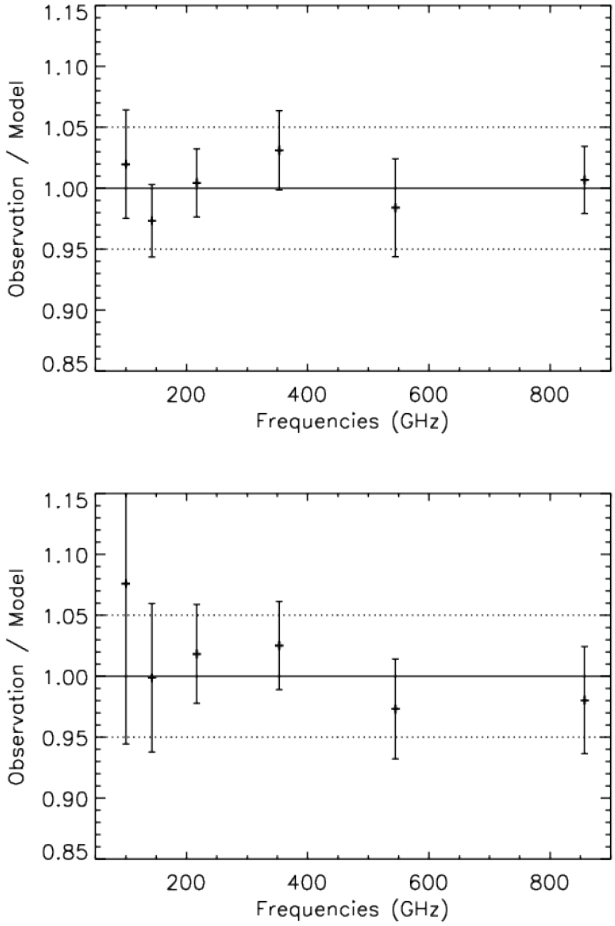

Figure 11. Ratio of the flux densities measured by HFI and computed from the ESA2 (Uranus) and ESA3 (Neptune) models from Moreno (2010), for Uranus (*top*) and Neptune (*bottom*). At 545 and 857 GHz, the measurements are not independent measurements of the planet flux densities, as the 545 and 857 GHz channels have been *re-calibrated* to match simultaneously the Uranus and Neptune flux densities given by the models.

5.3. Planet calibration uncertainties

At high-frequencies, we estimate the error on the absolute calibration for frequency maps to be of 10 % (for both the 545 and 857 GHz channels). This uncertainty combines the statistical uncertainty in the flux density measurements (5 %) to the systematic uncertainty in the Neptune and Uranus models, taken to be equal to 5 %. Note that the latter is probably overestimated as we have a very good relative calibration between the low-frequency channels (143, 217, 353 GHz), that have a much more accurate absolute calibration, and the high-frequency ones.

6. Setting the zero levels in the maps

At this stage the zero levels of the maps have not been set. *Planck* cannot fix them internally, we need to rely on the use of external datasets. The zero level comprises two parts:

– A Galactic zero level: we estimate the brightness in the *Planck*-HFI maps that corresponds to zero gas column density (zero gas column density means zero Galactic dust emission). As a gas tracer, we use the HI column density (21 cm emission) assumed to be a reliable tracer of the Galactic gas column density in very diffuse areas.
– An extragalactic zero level: the cosmic infrared background monopole.

The sum of the two offsets are appropriate for total emission analysis. For Galactic studies, only the Galactic zero level has to be set.

6.1. The Galactic zero level

Two methods were combined to obtain reliable numbers. The first one uses the correlation of the *Planck* maps with HI column density (21 cm emission). The basic idea is to estimate the brightness in the *Planck* maps that corresponds to zero column density by correlating with HI assumed here as a reliable tracer of the Galactic gas column density in diffuse areas (it thus neglects any dust associated with the diffuse HII gas that is not

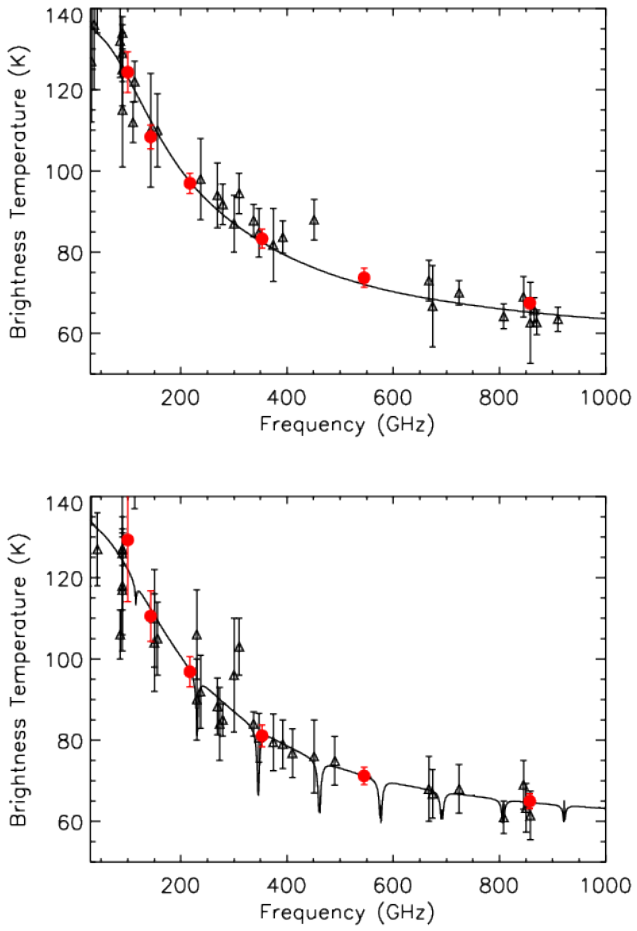

Figure 12. Variation of the brightness temperature with the frequency for Uranus (*top*) and Neptune (*bottom*). The brightness temperatures derived from the flux densities measured using aperture photometry on HFI maps are the *red points*. The continuous lines are the ESA2 (Uranus) and ESA3 (Neptune) models from Moreno (2010). The scale of the models is known at about 5 %, and the relative inter-frequency uncertainty is expected to be of the order of 2 %. At 545 and 857 GHz, the measurements are not independent measurements of the planet flux densities, as the 545 and 857 GHz channels have been *re-calibrated* to match simultaneously the Uranus and Neptune flux densities given by the models. The other data points are extracted from the literature.

spatially correlated with the HI). The model is simply:

$$I_\nu = \alpha_\nu \times N_{HI} + O_\nu \,. \tag{12}$$

The correlation with HI allows us to estimate O_ν independently for each frequency but it relies on the assumption of a tight gas-dust correlation over relatively large areas of the sky.

The second method is based on the inter-frequency correlation of *Planck* maps, where the model reads:

$$I_\nu = \alpha_\nu \times I_{\nu_0} + O_\nu \,, \tag{13}$$

where I_{ν_0} is one the *Planck* maps. Here the offsets are all relative to the offset of I_{ν_0} that needs to be determined otherwise (by the first method for instance). The advantage of this second method is that no assumption is made on the phase in which the gas is (we correlate dust emission with dust emission) and a larger area of the sky can be used to do the correlation. All the data were smoothed to a common angular resolution of 1°. CMB anisotropies as extracted in Planck Collaboration XII (2013) were also removed from the data prior to the correlation.

For the correlation with HI, we used the 21-cm all sky data from the LAB survey (Kalberla et al. 2005). The LAB data is the collection of close to 200 000 spectra that were processed individually. The map of HI column density used here is the assembly of those spectra in a sky cube, then summed over velocities. The zero level of the LAB data (and of 21 cm observations in general) depends mostly on the baseline subtraction at the spectrum level. At 1420 MHz, the spectroscopic observation is the sum of the 21 cm line, the synchrotron and free-free emissions, which are very well approximated by a power law at this frequency, and instrumental baseline variations due to various effects, including ground radio interferences and system temperature variations. The 21 cm emission is usually extracted by removing a baseline using a polynomial fit constrained with velocity channels away from the HI Galactic emission. The two radio-telescopes used to build the LAB data have a large velocity range coverage (from −450 to 400 km/s) allowing for a very good estimate of the baseline. In addition many sky positions were observed several times, allowing improvement on the baseline correction. Because the baseline correction is applied on each individual spectrum, the noise on the zero level will be at the pixel size on the final map and no bias at large angular scales should be expected. Larger scale zero level variations could come from stray (far-side lobe) radiation. The LAB data were constructed with the most precise stray-radiation correction to date, leaving very faint residual emission at a level of 40 mK, i.e., 7×10^{16} cm^{-2}, which is well beyond the zero level of the HI integrated emission map (3×10^{19} cm^{-2}). For the gain calibration, strong radio sources are used (S7, S8 and S9 in the case of the LAB data). The calibration is done regularly during observations to monitor any gain drift. The precision of the gain of the LAB data has no impact on the determination of the HFI zero level as it is obtained through a correlation.

The first method requires the use of a very strict mask, to include only regions where the gas is mostly in the neutral atomic form (no significant dark gas for example) and avoiding lines of sight with significant emission from clouds in the Galactic halo (Intermediate Velocity Clouds and High Velocity clouds) as they have slightly different dust emission properties. We select pixels where the local velocity cloud HI column density is $< 2 \times 10^{20}$ cm^{-2} and where no significant IVC emission is detected. This very strict mask includes 11.5 % of the sky. For inter-frequency correlations (Eq. 13) a second mask was built by including pixels where the local velocity clouds HI column density is $< 3 \times 10^{20}$ cm^{-2} (and no restriction on IVCs), increasing the sky fraction to 28 %.

To minimize the effect of the imperfect dust-HI correlation and to get the highest possible signal-to-noise ratio, the Galactic zero levels were computed using Eq. 12 at 857 GHz and using Eq. 13 at the other frequencies, thus taking $I_{\nu_0} = I_{857}$. We show in Fig 13 the 857 GHz-HI correlation. We observe a significant dispersion in the correlation, possibly due to variations of the dust-to-gas ratio, variations of the dust properties or due to the fact that HI is not a perfect tracer of column density (e.g., presence of dust in the warm ionised medium). Figure 14 shows an example of inter-frequency correlation, at 143 GHz. There is a

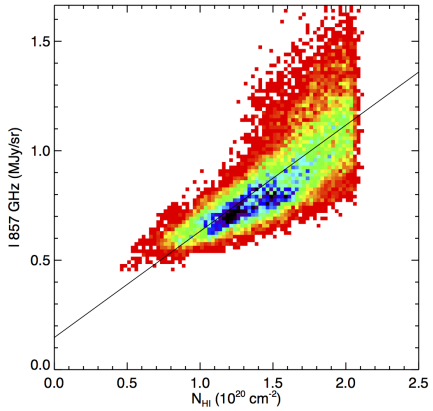

Figure 13. 857 GHz-HI correlation on 11.5 % of the sky ($N_{HI} < 2 \times 10^{20}$ cm^{-2} –smoothed to 1°– and outside intermediate velocity Clouds).

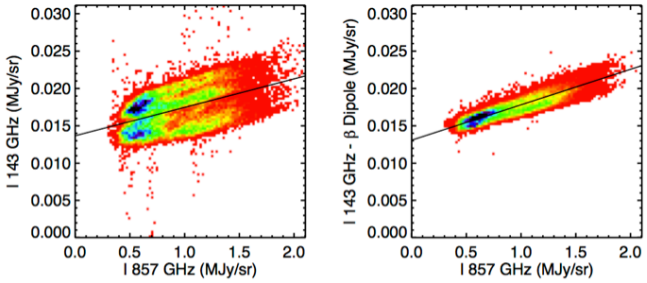

Figure 14. Correlation between the 143 and 857 GHz frequency map on 28 % of the sky (HI column density smoothed at 1° < 3×10^{20} cm^{-2}). CMB anisotropies have been removed at 143 GHz. *Left:* Raw correlation, *Right:* Correlation after a residual solar dipole has been removed at 143 GHz. The offset of this correlation sets the Galactic zero level of the 143 GHz map.

clear splitting in two of the correlation plots that reveals an effect unaccounted for in our model (Eq. 13). Once projected on the sky, the residual shows that the north and south parts of the mask have different offset values. This bi-modal structure is minimized once a residual solar dipole is removed from the data. To set the Galactic zero level, we thus also fit for the amplitude of a residual solar dipole by adding a solar dipole term in Eq. 13. The amplitude of this residual dipole pattern is in accordance with the actual accuracy of the absolute calibration (discussed in Sect 4.5). Indeed, with a given accuracy on the absolute calibration, a dipole with an amplitude of at least the given accuracy can be left in the map. We have no contradiction with the amplitude of the dipole left in the maps and the current absolute calibration uncertainties, listed in Table 11. More precisely, we found residual dipole amplitudes compatible with a 0.3 % calibration error for 100-217 GHz and 1 % for 353 GHz.

6.2. The cosmic infrared background monopole

The (istropic) mean value of the CIB is computed using the Béthermin et al. (2012) model. This is an empirical model based on the current understanding of the evolution of main-sequence and starburst galaxies. It reproduces very well the mid-infrared to radio galaxy counts. The values of the CIB (which is the integral of the galaxy numbers counts) have been computed using the HFI bandpass filters. They have then been converted into the convention νI_ν = cst using the CIB SED fit of Gispert et al. (2000). The values are given in Table 4. Errors are at the order of 20 %.The CIB has to be added to the maps for total emission analysis.

Table 4. CIB monopole that has to be added to the maps.

Frequencies [GHz]	CIB [MJy sr^{-1}] (νI_ν = cst)
100	3.0×10^{-3}
143	7.9×10^{-3}
217	3.3×10^{-2}
353	1.3×10^{-1}
545	3.5×10^{-1}
857	6.4×10^{-1}

Table 5. Table giving the offsets that have to be removed at each frequency to set the Galactic zero level. The offsets have been computed assuming zero Galactic dust emission for zero gas column density.

Frequencies [GHz]	DX9 maps [MJy sr^{-1}] (νI_ν = cst)	zodi-removed DX9 maps [MJy sr^{-1}] (νI_ν = cst)
100	0.0047±0.0008	0.0044±0.0009
143	0.0136±0.0010	0.0139±0.0010
217	0.0384±0.0024	0.0392±0.0023
353	0.0885±0.0067	0.0851±0.0058
545	0.1065±0.0165	0.0947±0.0140
857	0.1470±0.0147	0.0929±0.0093

6.3. Set the appropriate zero levels of HFI maps

The released maps have not been readjusted to zero at the levels of Table 5. For Galactic analysis, the Galactic zero levels, given in Table 5, have to be removed from the frequency maps. For total emission analysis, the CIB monopole, given in Table 4, also has to be added. As said previously, for the CIB we estimate the error to be at the order of 20 %. For the Galactic zero level, errors are given in Table 5. The uncertainty on the 857 GHz Galactic offset is dominated by systematics. At lower frequencies, the uncertainties take into account the impact of the CMB removal, the statistical uncertainty of the fit, and the error on the 857 GHz offset.

7. Characterisation and checks of calibration

We present in this section the various tests that have been done in order to assess the precision and stability of the calibration for the HFI data.

7.1. Time stability of the calibration

To evaluate the accuracy of the apparent gain variation correction by `bogopix` we compute, for a detector, the residual difference R between the HPR data d and a model including the destriping offsets o_r, the HFI I, Q and U maps, the dipoles t_D (orbital and Solar) and the calibration parameters (relative ring-by-ring gains from `bogopix`, noted g_r, overall gain based on the Solar dipole, noted G, and zero point derived as described

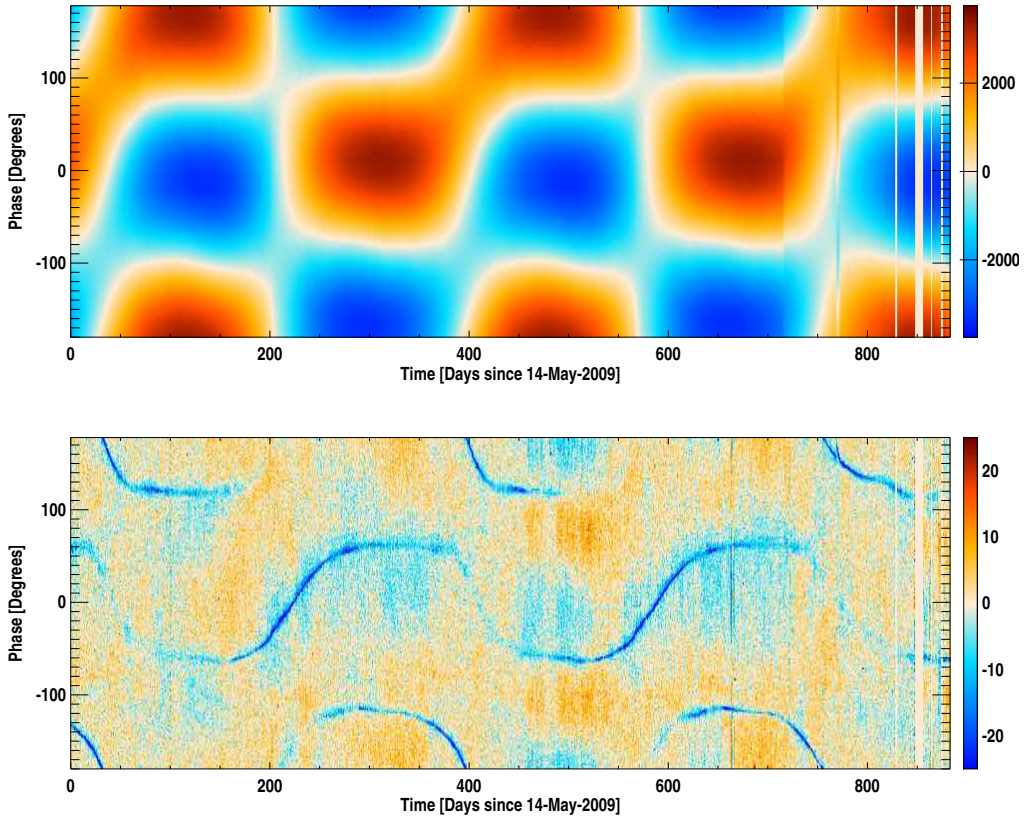

Figure 15. Distribution of the residuals in μK_{CMB}, computed as in Eq. 14, for detector 143-1a (bottom plot), in a (observation date, satellite rotation phase) representation. We compared this 2D image with the expected pattern for the Solar dipole, shown in μK_{CMB} by the upper plot, to check the level of residual gain variation after applying the `bogopix` gains.

above, noted z). This corresponds, for each HPR sample i of each ring r, and pixel p to :

$$R_i = (d_i - o_r)/(g_r \cdot G) - t_D - I_p - \rho \cos 2\psi_i Q_p - \rho \sin 2\psi_i U_p - z \quad (14)$$

We represent these residuals as a function of the rotation phase, computed as the angle between the direction of each pixel in the HPR with respect to the satellite velocity on Fig. 15. In this representation, the orbital dipole extrema will be found at fixed phases 0 and $\pm\pi$. The Solar dipole will present a modulated pattern, also illustrated on Fig. 15. As the solar dipole is the brightest component of the sky emissions, looking for its pattern in the residuals is a good indication of the inaccuracy of the gain variation correction. They may also capture addition time variable signals that would not be accounted for in our processing, for example the primary spillover pick-up. The areas where the Galactic emissions dominate show up as outliers in these residuals for several reasons. First, they correspond to regions were intra-pixel gradients are large, and will leave some imprints due to the individual scanning trajectories of each detectors. More importantly, they present emission spectra different from that of the CMB, on which we calibrate. Integrated over each detector's bandpass, this will translate into an apparent brightness difference. At this stage, we do not apply color-corrections to get rid of such effects, considering they can be largely minimized by a proper selection of the sky area (i.e., avoiding the Galactic plane area). Finally, imperfections in the time response of the detectors and in the pointing reconstruction will also induce larger residual in the Galactic plane. Masking these regions, using a 40 % Galactic mask, we checked that for all detectors from 100 to 217 GHz, the maximum level of the residuals we observe would correspond to a remaining gain variation lower than 0.3 % (i.e., they are lower than $\sim 10\,\mu K_{CMB}$).

7.2. Intra-frequency calibration checks

We checked the relative calibration of all detectors from a given frequency with each other on pseudo cross-power spectra. We start from the single detector temperature maps, neglecting polarization. We mask sky areas where the Galactic emissions are larger, keeping 40 % of the sky for frequencies lower than 300 GHz and 30 % above. We build the pseudo cross spectra of this set of maps, using Xspect (Tristram et al. 2005). We correct each pseudo spectrum for its beam window function (Planck Collaboration VII 2013). We then focus on the location of the first acoustic peak, so that results are not biased by beam uncertainties. For example, the set of spectra we get for the 143 GHz HFI detectors is shown in Fig. 16. We finally fit the recalibration coefficients that minimize the differences between these spectra, for ℓ in [25,300]. For 545 and 857 GHz we apply a color correction for the band-pass mismatch between detectors, assuming the *IRAS* spectral convention. The relative calibration coefficients found with this method should be considered as upper limits on the relative calibration precision of HFI, as we neglect polarization in this analysis. They are given for all frequencies in Table 6. For frequencies below 217 GHz the relative calibration accuracy is better than 0.4 %. These relative accuracies are consistent with the systematic uncertainties estimated in the previous section.

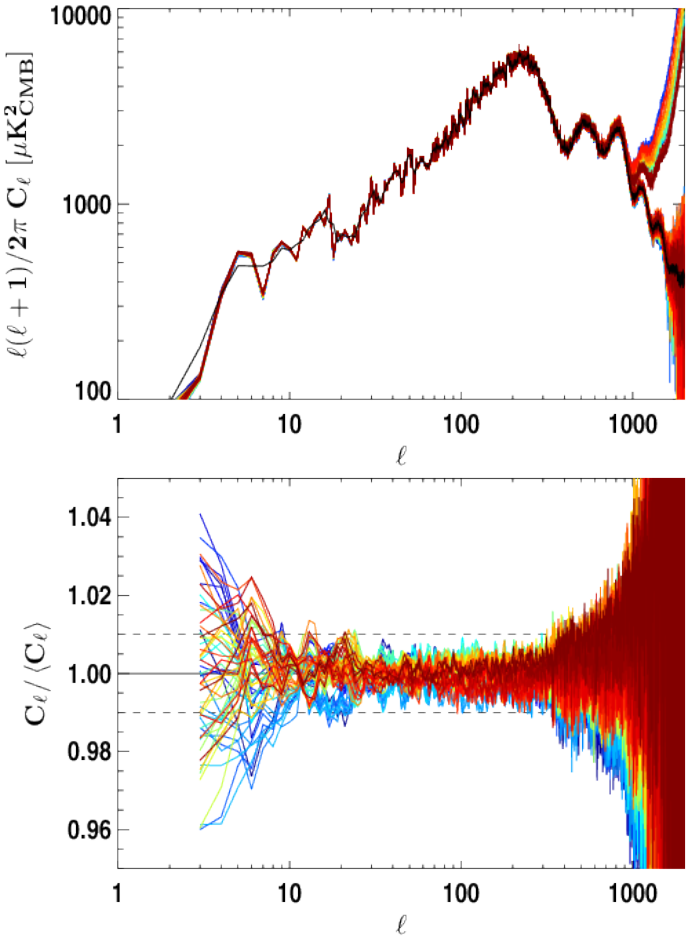

Figure 16. Auto and cross pseudo spectra obtained from the eleven 143 GHzHFI detectors corrected for the beam (top) and their ratio with respect to the average of the cross pseudo-spectra (bottom). This average is indicated in black in the top panel. Each detector pair is represented using a different colour. Note the noise suppression in the cross spectra, above $\ell \sim 800$.

Table 6. Maximum absolute value of the relative calibration coefficients fitted on pseudo spectra similar to those of Fig. 16, between detectors of each frequency. These values are thus upper limits of the relative calibration errors inside each channel (i.e., between all bolometers of a given channel).

Frequency [GHz]	100	143	217	353	545	857
Calibration [%]	0.39	0.28	0.21	1.35	1.3	1.4

We also compared the relative calibration coefficients derived from the pseudo cross spectra, for all 100, 143 and 217 GHz detectors, with the relative differences between gains based on Solar and orbital dipole calibration methods (see Sect. 4.3) in Fig. 17. Orbital dipole methods are both affected by the same systematics, the ADC non-linearities. CMB anisotropies are well intercalibrated between detectors, using Solar dipole calibration. This intercalibration would be worse with the orbital dipole based methods, except maybe at 100 GHz, which reinforces the choice of the Solar dipole calibration.

7.3. Inter frequency and absolute calibration checks for CMB dominated channels

In this section, we address the checks performed to study the calibration accuracy for CMB channels.

7.3.1. Pseudo cross spectra analysis

We applied a technique similar to what is presented in Sect. 7.2 to assess the HFI inter-frequency relative calibration for combined maps, at frequencies where the CMB dominates at high Galactic latitudes. We built pseudo power spectra from the temperature maps for 100, 143 and 217 GHz, applying a beam correction described in Planck Collaboration VII (2013). As above, we determine the cross calibration coefficients that minimize the difference between the cross pseudo power spectra of the HFI maps for ℓ in [25,300]. Results from this method are shown in Table 7. We see from these numbers that the internal relative calibration precision within HFI is better than ±.15 %.

Table 7. Cross calibration coefficients found when comparing the HFI frequency temperature maps with each other using cross-spectra. We report the coefficients minimizing the dispersion of the cross spectra arond their common mean.

Frequency [GHz]	100	143	217
Calibration	1.002	0.999	0.999

7.3.2. Solar dipole parameter fits

We also studied the calibration accuracy using fits of the CMB dipole parameters on HFI maps. To perform this test, we used maps built without dipole subtracion. Such fits are likely to be biased in presence of foregrounds, in particular due to the intrinsic dipole of the Galactic emissions. We therefore used a template fitting method to subtract dust emissions; our dust template is based on *IRAS* data (Neugebauer et al. 1984). We masked 10% of the sky, based on Galactic dust and CO emission, and point sources, before fitting the amplitude and direction of the CMB dipole. We present our results in Table 8. We retrieve the WMAP dipole amplitude measurement at 0.1 % or better in all cases. The direction, maybe more affected by foreground residuals, is reconstructed within $\sim 10'$. Those results are in agreement with the residual dipole measurements presented in Sect. 6.1, which might be more sensitive to foreground removal and masking.

Table 8. Differences between the CMB dipole parameters fitted on the HFI maps with those measured by *WMAP*. The typical statistical errors on these fits are ∼ 0.01 % for the amplitude and less than 1′ for the direction.

Frequency [GHz]	Amplitude [%]	Longitude [′]	Latitude [′]
100	−0.122	2.30	11.09
143	−0.074	3.00	11.91
217	−0.091	−5.10	12.79

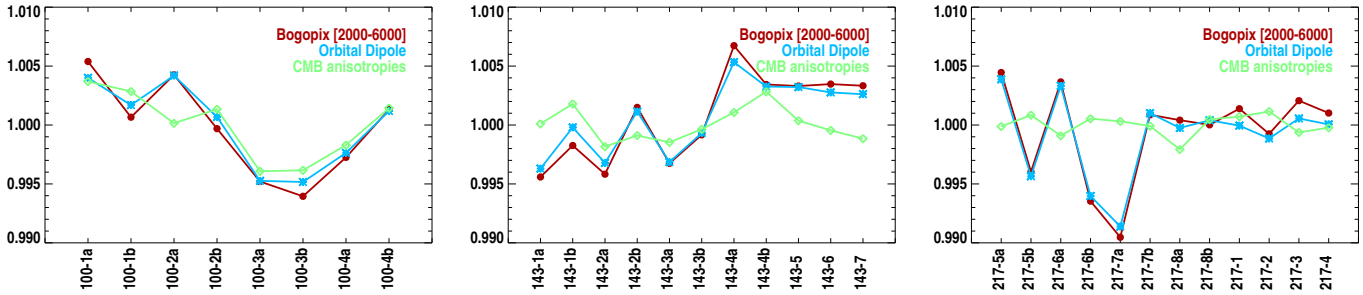

Figure 17. Relative calibration coefficients found when calibrating on the orbital dipole (constant gain : light blue, with `bogopix` in red) and using CMB anisotropies (see Sect. 7.2, in cyan), with respect to the Solar dipole gains, used to build the HFI maps. As ADC non-linearities are not corrected for, calibration systematics depend on the amplitude on the signal used to check for them. The amplitudes of such effects are within the systematic uncertainties quoted in Table 6.

7.3.3. Calibration checks using component separation methods

Finally, calibration consistency checks have been performed using component separation tools. In particular, the SMICA (Cardoso et al. 2008) component separation method has been used to fit relative calibration coefficients for each frequencies (including LFI data) on the CMB anisotropies (Planck Collaboration XII 2013). The foreground model is a non-parametric 4-dimensional model, meaning that the foregrounds are represented by four templates with arbitrary emission laws, arbitrary angular spectra and arbitrary correlations (2- and 3-dimensional fits where also performed with compatible results). Results from this test are summarized in Table 9. They agree, within error bars, with the results shown in Table 8 and Table 7. It should be noted that for frequencies above and including 353 GHz, Rayleigh scattering, not included in such studies, will distort the CMB anisotropies used to derive such cross-calibrations at a few percent level (Yu et al. 2001). So cross-calibration coefficients found for 353 and 545 GHz, which are of that order of magnitude, should be considered as estimation of systematic cross calibration uncertainties rather than genuine corrections of our maps. Such studies are routinely incorporated in *Planck* likelihood minimizations, so more results are shown in Planck Collaboration XV (2013). Comparison with LFI and WMAP, are developed in Planck Collaboration XI (2013).

Table 9. Cross calibration coefficients of the HFI sky maps at each frequency, with respect to the 143 GHz map, found with the SMICA component separation likelihood, with errors derived from Fisher matrix analysis.

Frequency [GHz]	Calibration –	Fisher Errors [%]
100	0.999	0.2
143	1	0.2
217	1.000	0.2
353	0.993	0.3
545	1.05	3.5

7.4. HFI/SPIRE cross calibration on diffuse emission

At high frequency, uncertainties on the SEDs of the astrophysical components together with their variability on the sky make extensive calibration checks as done in Sect. 7.1 and 7.3 more difficult to conduct. All that can be done is to study the cross calibration between HFI and other datasets, like SPIRE (Griffin et al. 2010). *Planck* HFI and the SPIRE instrument (on board *Herschel*) have two very close frequency channels: 857 GHz for the former versus 350 μm for the latter, and 545 GHz versus 500 μm. We used four very large SPIRE public fields (for a total of ~50 deg^2), with mean brightness ranging from 1.6 to 90 MJy sr^{-1} at 857 GHz, to compare the HFI and SPIRE brightness.

For each field we create SPIRE 350 and 500 μm maps using the Herschel Interactive Processing Environment pipeline HIPE v9.1. We applied the relative gain correction for extended emission and used the destriper module. SPIRE data are calibrated using Neptune and are given in Jy/beam for the convention νI_ν = cst. To convert the point source calibration to an extended emission calibration, we use the SPIRE beam solid angles of 822″ and 1768″ at 350 and 500 μm respectively, as advised by the most recent inputs on beams[4] . These values are also derived using the νI_ν = cst convention. SPIRE maps are then convolved with the HFI beam window function.

To compute the color corrections, we use the SPIRE Relative Spectral Response Functions (RSRFs)[5]. Due to the single-mode coupling via the feedhorns, SPIRE beams FWHM varies in ν^γ with frequency, where $\gamma = 0.85$ at both 350 and 500 μm (Griffin & al. 2013)[6]. In order to take this effect into account, we multiply the SPIRE RSRFs by $\nu^{-2\gamma}$ and renormalize it. Color correction factors, to convert SPIRE monochromatic flux densities into HFI-like monochromatic flux densities are computed assuming the real source spectrum is a modified blackbody of a given temperature and emissivity index: $B_\nu(T) \times \nu^\beta$. To estimate an average temperature per field we measure the 545/857 color using scatter plots (and we fix $\beta = 1.8$). We estimate the temperature dispersion as a departure

[4] https://nhscsci.ipac.caltech.edu/sc/index.php/Spire/PhotBeamProfileDataAndAnalysis

[5] https://nhscsci.ipac.caltech.edu/sc/index.php/Spire/PhotInstrumentDescription

[6] see also https://nhscsci.ipac.caltech.edu/sc/index.php/Spire/PhotBeamProfileDataAn dAnalysis

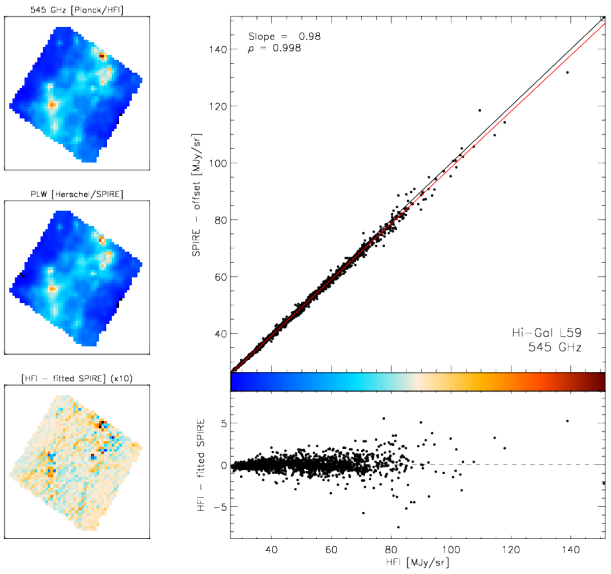

Figure 18. SPIRE/HFI pixel to pixel comparison in one 6 deg^2 "hi-Gal" field at 545 GHz. The red line is the result of a linear fit, the black line is a slope of unity. On the left are shown the HFI and SPIRE maps, together with the difference of the two. The difference is displayed between [-6.3,6.3] MJy/sr.

from the linear fit in each field expressed as a percentage of the 857 GHz brightness. It ranges from ∼2.5 % to ∼8 % depending on the field. This means that, while the average temperature and thus color correction factor is very robust, the temperature can locally vary by a few kelvins. In the worst case the estimated local temperature standard deviation gives a color correction variation of ∼1 %.

We estimate the agreement between the diffuse emission measurements from HFI and SPIRE by computing their correlation. An example of a scatter plot for one field and one frequency is shown in Fig 18. In all fields, HFI and SPIRE measurements correlate very well with an average Pearson correlation coefficient of 0.998. The dispersion across the linear fit ranges from ∼ 3 % to ∼ 8 % of the mean brightness of the field. We measure G_s = 0.98 and 0.93 at 545 and 857 GHz, respectively. At 545 GHz, the agreement between the HFI and SPIRE absolute calibration is excellent. At 857 GHz, we observe a systematic trend, with SPIRE being lower than HFI by 7 %. This is however inside the error bars of the two absolute calibrations that are 10 % for HFI (see Sect 4.5), and ∼7 % for SPIRE (see SPIRE observer manual[7]). Note that as of now it is fair to include the 5 % error on the model in the comparison as we use both Neptune and Uranus for the HFI calibration, and for Neptune we use a more recent model than that used currently for the SPIRE calibration ("ESA3" versus "ESA2"). A more detailed analysis on the comparison between the HFI and SPIRE absolute calibration will be presented in a forthcoming paper.

7.5. HFI maps noise levels assessment

When combining detector data to build frequency maps, we apply an inverse noise weighting scheme. The weights we use are derived from the noise levels measured from clean TOIs together with the calibration coefficients. The resulting noise level in the combined maps is therefore a consistency check of the relative calibration between detectors, as a mis-calibration would result in an additional noise given the slightly different scanning path and redundancies of the detectors.

We show in Fig. 19 the intensity maps that are reconstructed in each of the HFI frequencies, together with the number of TOI samples per pixel and two illustrations of the difference betweens maps built with the first and second half of each rings: the raw differences and the differences scaled by the square root of the number of TOI sample to pre-whiten them.

With respect to the HFI early data release, the detector noise estimation used for the detector's data weighting is slightly different for the 2013 data release than was was done for the previous release (Planck HFI Core Team 2011b). As a consequence, the pixel covariances we compute are coherent with noise levels estimated from the difference maps built from the first and second half of the rings.

Figure 20 presents pseudo-spectra of the null test difference maps, computed with a 15 % Galactic mask, for frequencies up to 353 GHz, and 40 % for the higher ones, combined with a point source mask derived from the *Planck* catalogue. We compared these spectra on Fig. 20 with those from the half difference of the maps reconstructed from surveys 1 and 2 properly normalized to compensate the lower integration time. As illustrated previously on Fig. 4 such differences are sensitive to, among others, calibration apparent time variation. As they compare observations made with roughly opposite scan directions, they may also exhibit residuals in regions where the sky signal is intense, and large gradients due to time response imperfect deconvolution (Planck Collaboration VI 2013). As a consequence, their spectra, shown as dashed lines on Fig. 20, present an increase at low multipole with respect to those of the half ring differences. The fact that both half difference spectra are very close to each other at high multipole, for frequencies lower than 353 GHz, is an indication that they provide an estimation of the high spatial frequency part of the noise included in the HFI 2013 data release. For the sub-mm channels, both spectra present a significant ℓ variation, showing they are contaminated by systematic residuals.

We derive from these pseudo-spectra estimation of the noise level on the HFI maps by computing their average, after their re-normalisation by the sky coverage, in the ℓ range [100-6000]. Using the averaged hit count per pixel, we convert these averages into an equivalent r.m.s per TOI sample. We compare this estimation with two other estimators: the r.m.s of the half ring map differences, properly whitened using the hit counts, and the averaged squared root of the variance computed in each pixel by the projection module, scaled to a dispersion per TOI sample using the averaged hit counts. These estimations are compared in Table 10. In general, they are in fair agreement for the three lowest frequencies, indicating that they provide a good estimation of the noise level in the maps. At higher frequencies, however, signal residuals have a larger contributions. Therefore, such methods only provide an upper limit of the high frequency noise in the maps.

8. Conclusions

We presented in this paper the mapmaking and calibration for the *Planck* High Frequency Instrument data for the 2013 release. The calibrator for the CMB frequency data (100-353 GHz) is the Solar dipole anisotropies as measured by *WMAP* (Hinshaw et al.

[7] http://herschel.esac.esa.int/Docs/SPIRE/html/spire_om.html

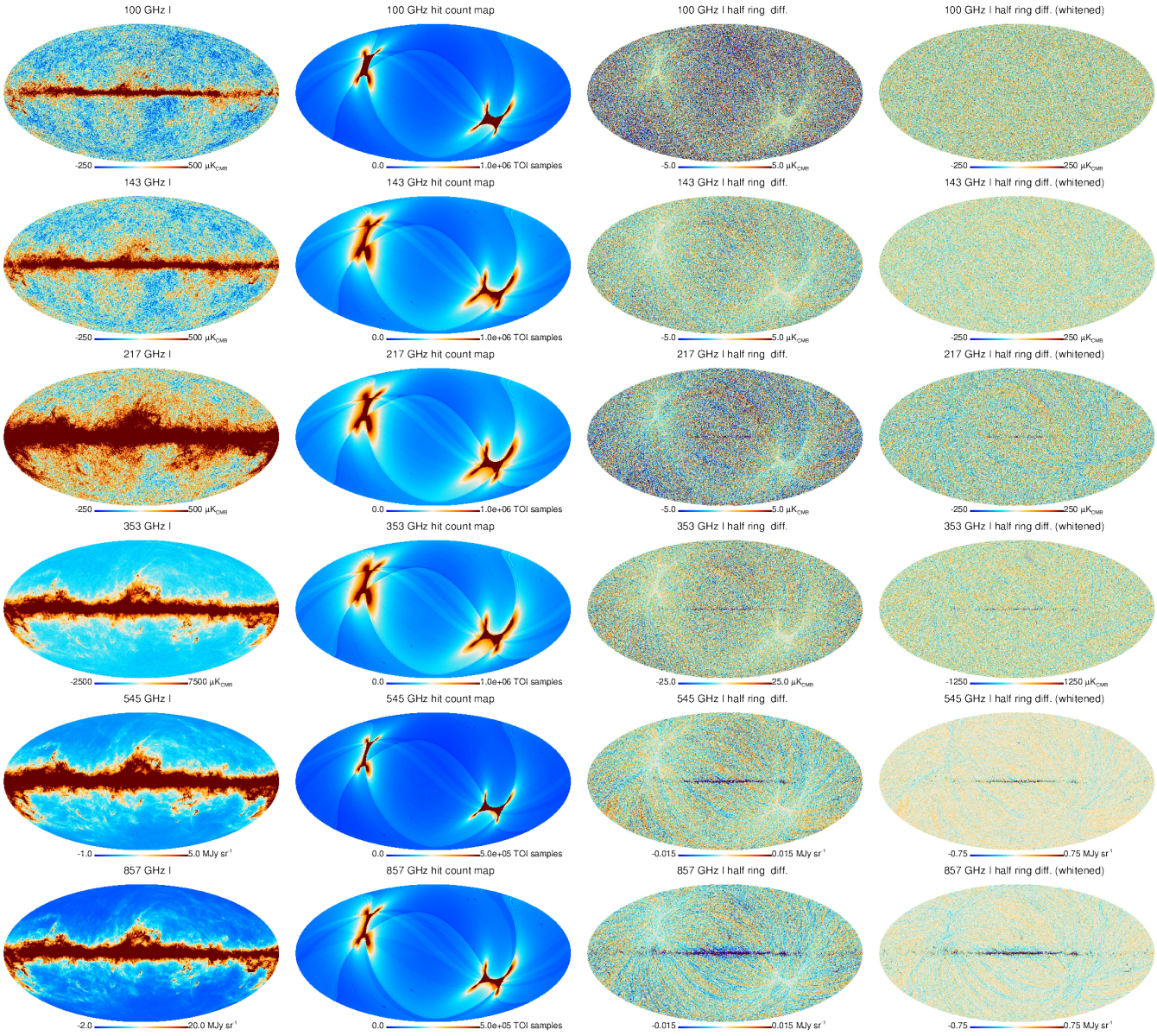

Figure 19. Signal (left), hit counts (center) and half differences between maps built with only the first and second half of each ring (right) for all HFI frequencies. The last column shows the half ring difference maps, scaled by the squared root of the number of TOI samples, which largely removes this correlation. For the two highest frequencies, the differences present residual stripes and signal artefacts, at a low level (below 1 %) with respect to the sky signal. The differences maps have been degraded to the $Nside = 128$ HEALPix resolution.

2009). This calibration is performed through a ring by ring template fit. Its limitations are consequences of the non-ideal behaviour of the ADC from the bolometer read-out electronics. Tiny deviations from linearity in these devices are causing apparent variation of the detector chain with time, which we have been addressing using a effective gain correction, `bogopix`. We showed that this scheme was able to reduce the apparent gain variation in time from 1 to 2 % to lower than 0.3 % by studying the residual of the map reconstruction with time. Higher order signal distortions induced by this systematic effect prevent us from using the precise, orbital dipole based, calibration scheme presented in Tristram et al. (2011).

Correcting for these ADC non linearities should be made prior to any data reduction step. It requires precise measurements of each ADC response, which is currently taking place using warm data. First tests of corrective software are also under way, with promising results.

The calibration for the 545 and 857 GHz is performed by comparing Uranus and Neptune flux densities with models of their emissivities. We had to switch to this scheme due to apparent systematic effects in the FIRAS spectra we used in the HFI Early Data release. At those frequencies, gain variations are lower than the other systematic calibration uncertainties.

We revised our zero level setting method, which now relies on the CIB monopole and the zero of the Galactic emission defined as zero dust emission for a null HI column density.

The statistical uncertainty of the calibration is negligible for all frequencies with respect to the systematic uncertainties. The systematic uncertainty has been evaluated using several methods, presented in Sect. 7. We evaluated three types of systematic uncertainties :

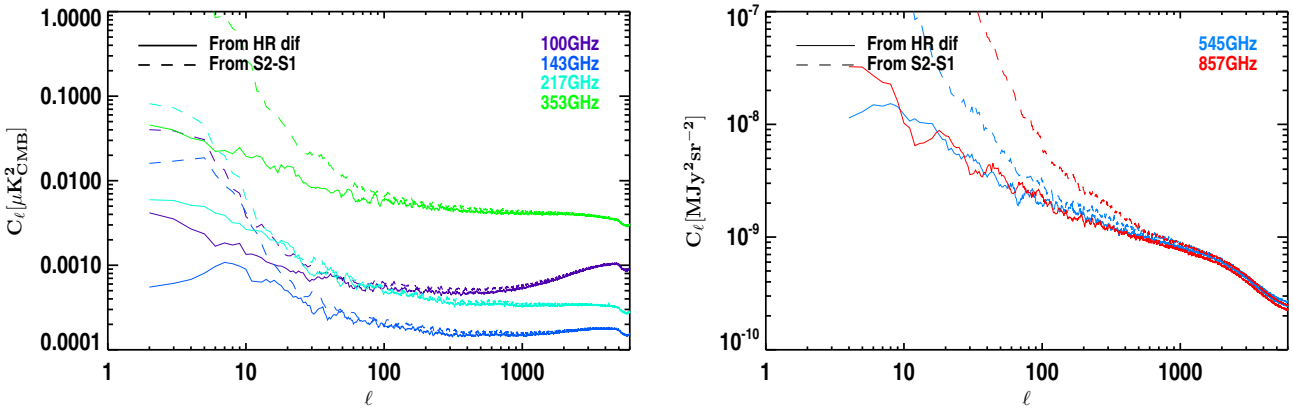

Figure 20. Pseudo-spectra reconstructed from the half differences between maps from the first and the second half of each rings (plain lines) and the half differences between maps restricted to survey 1 and 2 (dashed lines) for respectively the dipole calibrated channels (right) and the sub-millimetre ones (right). These pseudo-spectra were computed using galactic masks removing 15 % (CMB channels) and 40 % (sub-mm channels) of the sky respectively, combined with the Planck point source mask. For high frequency channels, power spectra are dominated by signal and destriping residuals, due to gradients inside the pixels, which are not scanned exactly at the same position between the two datasets. In the survey differences, other systematics like time response, pointing drifts and calibration time instability also induce larger residuals.

Table 10. Results of the three methods for deriving the TOI r.m.s. per sample from (a) the variance maps, (b) the r.m.s of the half ring difference maps and (c) the pseudo spectra from Fig. 20, as explained in the text, for each frequencies. Units are μK_{CMB} for 100 to 353 GHz, and MJy sr^{-1} [νI_ν = cst] for the sub-mm channels. These results should be considered as rough estimates only. The higher the frequency, the larger are the contributions for systematics residuals in the half differences like time constant, signal gradients.

Frequency [GHz]	Variance maps (a)	Diff. maps (b)	Pseudo-spectra (c)
100	1569	1546	1554
143	777	775	826
217	1109	1105	1212
353	3671	3712	4101
545	0.604	0.976	0.817
857	0.695	2.58	0.920

(a) *Residual apparent variations of gains with time*. For the 100 to 217 GHz maps, we showed in Sect. 7.1 that, using `bogopix` these variations where lower than 0.3 %, at detector level. As shown in Fig. 9 the apparent gain variations appear to be independent from one detector to the other, so such uncertainties should average out in the combined maps from this release. This 0.3 % uncertainty is therefore a conservative upper limit on the level of residual gain variations in the frequency maps. At higher frequencies, no estimation nor correction for the apparent gain variations is available. We choose to quote the level of variations we observed in the single detectors' measurements of `bogopix` at lower frequencies, which is 1 %; this is again an upper limit for combined maps. Given *Planck*'s scanning strategy, such uncertainties might be relevant for point-like sources studies, as these are observed in general once per survey, or globally when comparing sky maps from individual surveys.

(b) *Relative calibration uncertainties*, which should be used when combining several frequency maps with each other e.g., when reconstructing the SED of an object. We presented in Sect. 7.3 several methods to evaluate such uncertainties, for CMB channels. Both a direct comparison of pseudo power spectra outside the Galaxy and results from the component separation method SMICA show that the inter-calibration between the 100 to 217 GHz is better than 0.2 % (we keep the more conservative estimate, the SMICA errors). We complement these results with the upper limits extracted from SMICA results at 353 GHz, using the central value as upper limit of the uncertainty, and, for the relative calibration of the 857 GHz maps, the 5 % uncertainty on the photometry used in the planet calibration.

(c) *Absolute calibration uncertainties* that should be considered when comparing with other datasets. This involves comparing *Planck* data with an external calibrator. For CMB channels, such uncertainties have been evaluated by two complementary approaches: reconstructing the dipole and comparing it with the WMAP measurements (Sect. 7.3) or evaluating the amplitude of residual dipoles in our maps, after foreground removal (Sect. 6). Both methods show, from 100 to 217 GHz, a consistency with WMAP at better than 0.3 %; the second shows an agreement at 1 % for 353 GHz. As we are calibrated on the WMAP dipole measurement, an additional uncertainty of 0.24 % has to be combined with the HFI intrinsic systematics. For the two highest frequencies, the absolute scale is limited by that of the planets atmosphere models (5 %), combined with systematic uncertainties in our flux measurements (5 %), which results in a total uncertainty of 10 %. Such uncertainties are relevant for comparing *Planck* data with other datasets. When comparing with datasets sharing the same calibrator than HFI, *WMAP* dipole or the planet models of Moreno (2010), the uncertainty on these calibrator should therefore be omitted in the comparison.

We summarize the calibration uncertainties for the HFI frequency maps in Table 11.

Acknowledgements. The development of *Planck* has been supported by: ESA; CNES and CNRS/INSU-IN2P3-INP (France); ASI, CNR, and INAF (Italy);

Table 11. Summary of the HFI systematic calibration uncertainties for the frequency maps of the 2013 data release. Column (a) gives the residual relative calibration due to time variation that may be present in the data, (b) gives the relative calibration uncertainty from one HFI channel to the other and (c) the absolute calibration uncertainties of each HFI channel, including the uncertainty of the calibrators. The contents of columns (a), (b) and (c) are described in detail in the text. We indicate in the last column the uncertainties of the calibrators (*WMAP* dipole and models of planets) that are already included in the absolute uncertainties listed in column (c). These have to be taken into account when comparing with datasets relying on the same calibrators.

Frequency [GHz]	Time stability (a) [%]	Relative (b) [%]	Absolute (c) [%]	Model [%]
100	0.3	0.2	0.54	0.24
143	0.3	0.2	0.54	0.24
217	0.3	0.2	0.54	0.24
353	1.	1.	1.24	0.24
545	1.	5.	10.	5.
857	1.	5.	10.	5.

NASA and DoE (USA); STFC and UKSA (UK); CSIC, MICINN and JA (Spain); Tekes, AoF and CSC (Finland); DLR and MPG (Germany); CSA (Canada); DTU Space (Denmark); SER/SSO (Switzerland); RCN (Norway); SFI (Ireland); FCT/MCTES (Portugal); and PRACE (EU). A description of the *Planck* Collaboration and a list of its members with the technical or scientific activities they have been involved into, can be found at http://www.rssd.esa.int/index.php?project=PLANCK&page=PlanckCollaboration.

References

Ashdown, M. A. J., Baccigalupi, C., Bartlett, J. G., et al. 2009, A&A, 493, 753
Béthermin, M., Daddi, E., Magdis, G., et al. 2012, ApJ, 757, L23
Cardoso, J., Martin, M., Delabrouille, J., Betoule, M., & Patanchon, G. 2008, IEEE Journal of Selected Topics in Signal Processing, 2, 735, special issue on Signal Processing for Astronomical and Space Research Applications
Dame, T. M., Ungerechts, H., Cohen, R. S., et al. 1987, ApJ, 322, 706
Finkbeiner, D. P., Davis, M., & Schlegel, D. J. 1999, ApJ, 524, 867
Fixsen, D. J., Dwek, E., Mather, J. C., Bennett, C. L., & Shafer, R. A. 1998, ApJ, 508, 123
Fixsen, D. J., Weiland, J. L., Brodd, S., et al. 1997, ApJ, 490, 482
Gispert, R., Lagache, G., & Puget, J. L. 2000, A&A, 360, 1
Górski, K. M., Hivon, E., Banday, A. J., et al. 2005, ApJ, 622, 759
Griffin, M. J., Abergel, A., Abreu, A., et al. 2010, A&A, 518, L3
Griffin, M. J. & al. 2013, in prep.
Hinshaw, G., Weiland, J. L., Hill, R. S., et al. 2009, ApJS, 180, 225
Kalberla, P. M. W., Burton, W. B., Hartmann, D., et al. 2005, A&A, 440, 775
Kamionkowski, M. & Knox, L. 2003, Phys. Rev. D, 67, 063001
Lagache, G., Abergel, A., Boulanger, F., Désert, F. X., & Puget, J.-L. 1999, A&A, 344, 322
Liang, Z., Fixsen, D. J., & Gold, B. 2012, ArXiv e-prints
Lindal, G. F. 1992, AJ, 103, 967
Macías-Pérez, J. F., Lagache, G., Maffei, B., et al. 2007, A&A, 467, 1313
Maffei, B., Noviello, F., Murphy, J. A., et al. 2010, A&A, 520, A12+
Mather, J. C., Fixsen, D. J., Shafer, R. A., Mosier, C., & Wilkinson, D. T. 1999, ApJ, 512, 511
Moreno, R. 2010, Neptune and Uranus planetary brightness temperature tabulation. Tech. rep., ESA Herschel Science Center, available from ftp://ftp.sciops.esa.int/pub/hsc-calibration/PlanetaryModels/ESA2
Moreno, R., Lellouch, E., Lara, L. M., et al. 2011, A&A, 536, L12
Murphy, J. A., Peacocke, T., Maffei, B., et al. 2010, Journal of Instrumentation, 5, 4001
Neugebauer, G., Habing, H. J., van Duinen, R., et al. 1984, ApJ, 278, L1
Perdereau, O. 2006, in CMB and Physics of the Early Universe
Planck Collaboration I. 2013, In preparation
Planck Collaboration II. 2013, In preparation
Planck Collaboration IX. 2013, In preparation
Planck Collaboration V. 2013, In preparation
Planck Collaboration VI. 2013, In preparation
Planck Collaboration VII. 2013, In preparation
Planck Collaboration XI. 2013, In preparation
Planck Collaboration XII. 2013, In preparation
Planck Collaboration XIV. 2013, In preparation
Planck Collaboration XV. 2013, In preparation
Planck Collaboration XVIII. 2011, A&A, 536, A18
Planck Collaboration XXVIII. 2013, In preparation
Planck HFI Core Team. 2011a, A&A, 536, A4
Planck HFI Core Team. 2011b, A&A, 536, A6
Puget, J.-L., Abergel, A., Bernard, J.-P., et al. 1996, A&A, 308, L5
Reach, W. T., Dwek, E., Fixsen, D. J., et al. 1995, ApJ, 451, 188
Silverberg, R. F., Hauser, M. G., Boggess, N. W., et al. 1993, in Society of Photo-Optical Instrumentation Engineers (SPIE) Conference Series, Vol. 2019, Society of Photo-Optical Instrumentation Engineers (SPIE) Conference Series, ed. M. S. Scholl, 180–189
Tauber, J. A., Norgaard-Nielsen, H. U., Ade, P. A. R., et al. 2010, A&A, 520, A2
Tristram, M., Filliard, C., Perdereau, O., et al. 2011, A&A, 534, A88
Tristram, M., Macías-Pérez, J. F., Renault, C., & Santos, D. 2005, MNRAS, 358, 833
Wright, E. L., Mather, J. C., Bennett, C. L., et al. 1991, ApJ, 381, 200
Yu, Q., Spergel, D. N., & Ostriker, J. P. 2001, ApJ, 558, 23

Appendix A: HFI and FIRAS data comparison

The procedure we used for comparing HFI and FIRAS data is very similar to what was adopted by the ARCHEOPS collaboration (Macías-Pérez et al. 2007). It has been briefly described in Planck HFI Core Team (2011b). Here we give the full details of the comparison.

A.1. FIRAS data: spectra and derived maps

FIRAS spectra – The FIRAS instrument, its operating modes, calibration, and the data products are described in detail in the FIRAS Explanatory Supplement (FIRAS team, 1997, http://lambda.gsfc.nasa.gov/product/cobe/firas_exsupv4.cfm). Briefly, the FIRAS is a scanning, four-port (two inputs; two outputs) Michelson interferometer that uses polarizing grids as beamsplitters and creates an interferogram (i.e., the Fourier transform of the source spectrum) by scanning a movable mirror platform (the 'Mirror Transport Mechanism', or MTM). A dichroic splitter at each output port (arbitrarily designated "left" and "right") further splits each beam into low (30 - 630 GHz) and high (600 - 2910 GHz) frequency bands. The MTM can be scanned at either of two speeds: "slow" or "fast". And the MTM sweep can be set to one of two scan lengths, "long" or "short," thus affecting the spectral resolution.

Most research applications call for one or more high-level products as the dust spectrum maps that we are using here. In these high-level products, the different modes and detector signals were rejoined to form the HIGH and LOWF frequency data-set. The two dust spectrum maps (FIRAS_DUST_SPECTRUM_HIGH.FITS and FIRAS_DUST_SPECTRUM_LOWF.FITS) cover 98.7 % of the sky and give the residual sky spectrum, from ~105 to 4400 μm, after modeled emission from the CMB, interplanetary dust, and interstellar lines have been subtracted. The remaining signal is thus dominated by thermal continuum emission from Galactic interstellar dust (and extragalactic IR background e.g., Puget et al. (1996), Lagache et al. (1999), Fixsen et al. (1998)).

Uncertainty estimates – Uncertainties in the FIRAS data come from many different sources and manifest themselves in many

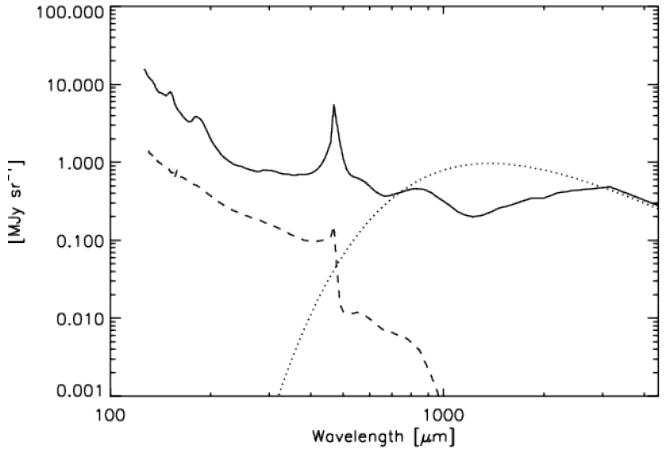

Figure A.1. FIRAS uncertainty summary. Only the uncertainties relevant to our purpose are displayed here (continuous line: the C-vector, dashed line: JCJ gain multiplied by the average sky spectrum and dotted line: the PTP uncertainty).

different ways. Fortunately, many of the uncertainties are quite well described by a few dominant terms that show the source of uncertainty. All of them are fully detailed in the FIRAS explanatory supplement (FIRAS team, 1997). The errors are divided into groups: the detector measurements, the calibration emissivities, the bolometer model parameters, the temperature measurements of all but XCAL (XCAL is the external Calibrator) and the temperature measurement of the XCAL. For our purpose, only the detector noise, the uncertainties in some parameters derived from the calibration and the uncertainty in the absolute temperature scale of the external calibrator are of importance. The covariance matrix writes as:

$$V = C + JCJ\_GAIN + PTP\_SPEC \quad (A.1)$$

where,

- the C-matrix is the detector noise (it includes off-diagonal terms due to frequency correlations introduced by the apodization of the coadded interferograms before Fourier transformation into spectra),
- the JCJ term corresponds to uncertainties linked to the bolometer model parameters (only the JCJ gain is important here). This error is considered as a systematic error,
- the PTP term is the absolute thermometry uncertainty. The PTP error is not a statistical uncertainty. It is included in the error budget since it is the dominant error for the absolute temperature of the Cosmic Microwave Background Radiation. It is thus important for comparisons of FIRAS measurements to other experiments (but only for wavelengths larger than ~700μm).

The level of these three uncertainties are shown on Fig. A.1. For the detector noise, only the square root of the diagonal (the 'C-vector') is displayed.

In Fixsen et al. (1997), they used a conservative estimate of the gain uncertainty of 2 % for the 20-80cm^{-1} FIRAS data.

Building FIRAS maps – For individual pixels at high Galactic latitude, the S/N ratio of FIRAS spectra is about 1. Of course, this is not the case in the Galactic plane where the S/N ratio is ~50 times higher (at high frequencies). The FIRAS map at one selected frequency can be obtained by convolving the FIRAS spectra with the *Planck*-HFI bandpass filters. However, this method gives very noisy FIRAS maps at high Galactic latitude (especially for $\lambda > 700$ μm). Since we are interested by both the Galactic plane and its surrounding, we have preferred to derive the FIRAS maps together with their errors using fits of FIRAS spectra. Each individual FIRAS spectrum is fitted with a black body modified by a ν^β emissivity law:

$$S_\nu = \tau \left(\frac{\nu}{\nu_0}\right)^\beta P(\nu, T_{dust}) \quad (A.2)$$

where τ is a measure of the relative dust column density for each pixel, β is the spectral index and $P(\nu, T_{dust})$ is the Planck function. Since we are searching for the best representation of the data and not for physical dust parameters, we neglect the contribution of the Cosmic Infrared Background. We moreover restrict the fit to the frequency range of interest – this avoids the need of a second dust component as in Finkbeiner et al. (1999).

For each frequency needed for the calibration, we find the best value of τ, T_{dust}, and β using a χ^2 minimization method for each pixel. We include correlations between frequencies of FIRAS spectra, and perform the fit on frequency intervals related to each needed frequency. We compute the errors in each pixel by considering the deviation of the emissivity induced by all models (Eq. 2) allowed at 68 % confidence level by the FIRAS spectrum fit. Only the C-matrix was considered. The JCJ and PTP term are added as a systematic error at the end of the process.

Ideally, fits have to be done on independent frequency intervals so that the maps derived at the *Planck*-HFI wavelengths are independent. However reducing the frequency interval increases the noise. Moreover, FIRAS data are too noisy at long wavelengths to perform the fits on small frequency intervals centered on the *Planck*-HFI wavelengths. As a consequence, the frequency intervals although shifted towards longer wavelengths as the *Planck*-HFI wavelengths increase do overlap. We have made extensive tests to derive the minimum and maximum frequencies to be taken for the fits. Fortunately, the choice of the boundaries is not critical for the result of the fit – there are no systematic effects and the values derived at the *Planck*-HFI wavelengths are highly consistent. This is not the case for the error bars that can vary by factors of 2. We show on Fig. A.2 results of the fits for three different pixels. Fits are done for 170< λ <530 μm, 200< λ <750 μm, 300< λ <1100 μm, 350< λ <1800 μm and 450< λ <4000 μm for the 350, 545, 850, 1380 and 2090 μm *Planck*-HFI wavelengths, respectively. Typically, for galactic latitudes $|b| < 5°$, the median 1σ represent 1.0, 1.5, 4.2, 9.8 and 35.1 % at 350, 545, 850, 1380 and 2090 μm, respectively. For $15° < |b| < 20°$, they reach 5.5, 11, 29, 54, and 158 %, respectively.

A.2. *Planck*-HFI data: towards the FIRAS resolution

We build uncalibrated *Planck* maps for each detector, and convolved them with the FIRAS beam.

FIRAS beam – The FIRAS beam has been measured using the moon. Due to imperfection in the sky horn antenna, the effective beam shows both radial and azimuthal deviations from the nominal 7° top hat beam profile (Fig. A.3). Since *COBE* rotates about

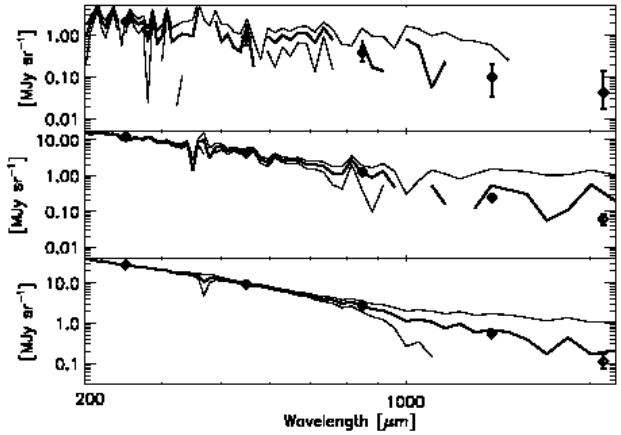

Figure A.2. Example of FIRAS spectra (with their $\pm 1\sigma$ error) with the computed values at the *Planck*-HFI wavelengths.

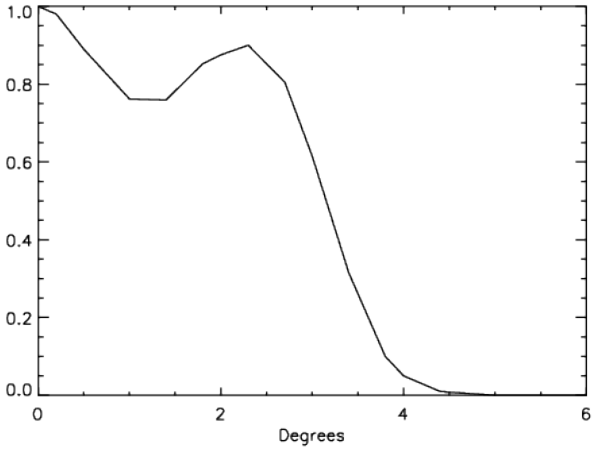

Figure A.3. FIRAS beam profile.

the optical axis of the FIRAS instrument, on average, the beam must have cylindrical symmetry. However, the time it takes to collect a single interferogram is less than a rotation period. Thus, a particular measurement beam may be asymmetric. Fixsen et al. (1997) estimate that the assumption of beam symmetry may produce residual beam shape errors of order of 5 % (see how we propagate this error).

Convolution – We do the beam convolution in the HEALPix scheme. To simulate the movement during an integration of an interferogram, the DIRBE-format data were further convolved by a 2.°6 tophat in the direction perpendicular to the ecliptic plane (which is roughly the FIRAS scanning direction).

A.3. FIRAS data: towards the HEALPix projection

Planck data are presented in the HEALPix format (Górski et al. 2005) with a resolution of the HEALPix grid $N_{\rm side} = 2048$. To be compared to the FIRAS data, the convolved-HFI maps are downgraded to $N_{\rm side} = 32$.

COBE data are presented in a quadrilateralized spherical projection (the so-called *COBE* Quadrilateralized Spherical Cube, CSC), an approximately equal-area projection in which the celestial sphere is projected onto an inscribed cube. Unlike the Aitoff, Molweide, and Global-sinusoidal projections, the "quad-sphere" projection does not have polar singularities. A disadvantage is that there is no standard way to present data in the quad-cube projection in a FITS file. The FIRAS convention is to divide each cube face into 32×32 pixels, leading to a total of 6144 pixels (of $\sim$ 2.°6). To be compared with *Planck*, FIRAS maps are put in the HEALPix format using a drizzling re-projection code.

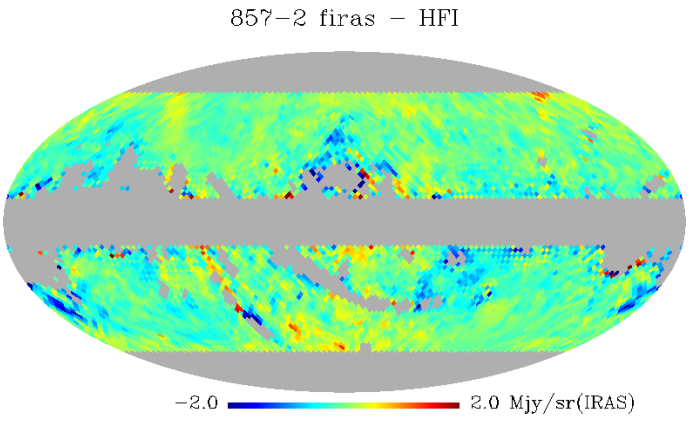

Figure A.4. FIRAS minus convolved-HFI for the 857-2 detector (in MJy/sr). Only pixels used for the "nominal" calibration are shown (i.e., $10° < |b| < 60°$, outside the CO mask, and pixels with enough FIRAS coverage)

A.4. Deriving the calibration gains and zero points

We fit for the calibration coefficients K and O following:

$$F(\nu_0)/cc = K \times HFI(\nu_0) + O \qquad \text{(A.3)}$$

where $F(\nu_0)$ is the FIRAS brightness at ν_0, and $HFI(\nu_0)$ is the HFI signal in pW at ν_0. K is the gain calibration factor, given for a source spectrum with νI_ν = cst, and cc is the color correction given in Eq. 1. The calibration coefficients K and O are derived from a linear fit of the FIRAS and HFI cosecant variations, restricted to intermediate Galactic latitudes ($10° < |b| < 10°$). We avoid using the inner part of the Galactic plane, as in these areas the spectral characteristics averaged out in the FIRAS measurements may present angular scale variations that are not accurately accounted for in our processing of the HFI data (i.e., we consider K and cc at 7° and not at 5′). More importantly, we avoid the inner part to minimize the effect of the FIRAS beam uncertainties. The Galactic polar caps are also not used, since the S/N ratio of the FIRAS data extrapolation is very low in such areas. We also mask regions where CO emission lines (removed from FIRAS measured spectra) are too bright using the Dame et al. (1987) map, and add a template of CMB anisotropies to the FIRAS data.

We use Eq. A.3 to fit for both the gain and the offset for all HFI detectors, and use the measured offset to compute the zero levels. Statistical errors are dominated by the FIRAS errors (HFI errors negligible). The error on O is dominated by the systematic effect observed on the gain K (see next section). We use the dispersion of the fitted values in the different parts of the

Table A.1. Error on the zero points (in MJy sr^{-1}[νI_ν = cst]).

Detector	Statistical	Systematic	Sum
857-1	0.23	2.40	2.63
545-1	0.67	0.65	1.32
353-1	0.57	1.78	2.25
217-1	0.57	1.08	1.65
143-5	0.61	0.66	1.27
100-1a	0.85	0.42	1.67

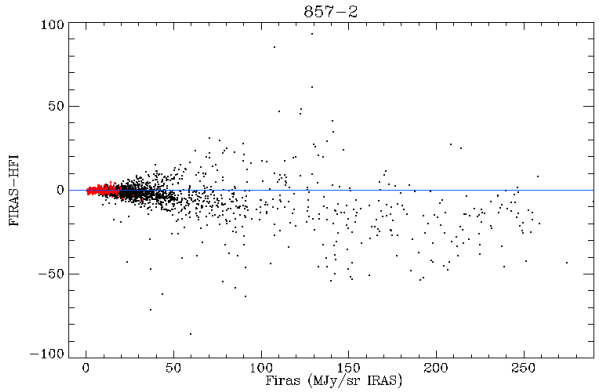

Figure A.5. Scatter plot FIRAS minus convolved-HFI versus FIRAS. We see that in average the difference goes more negative as the brightness in increasing. The red points are those used to compute the nominal calibration coefficients. We see for the high brightness data points that HFI is overestimated with respect to FIRAS.

sky to estimate the systematic error. This error is about 3 % at 857, 5 % at 545, 5 % at 353 and 10 % at 143 GHz. At 217 and 100 GHz, since we have no way to address the real variations without removing the CO contamination, we also take 10 % as the systematic errors. For the total error on O, we linearly sum the statistical and systematic errors. Errors for some individual bolometers are given in Table A.1).

Using the frequency maps and the component separation in the CIB fields, we can compute the CIB mean value in those fields and compare them to the expected values (see Table A.2). Although the error bars on the measured CIB at low frequencies are quite large, we see a systematic trend: the CIB is systematically lower than the expected CIB (factor of 2.4, 2, 1.4 and 1.5).

An example of residual map is shown on Fig. A.4. We see that on the sky area chosen to compute the calibration coefficients, the residual is close to zero except nearby bright regions (e.g., the Taurus cloud) where the FIRAS brightness is underestimated compared to HFI.

A.5. Systematic effects in the calibration coefficients

Since the early times of the *Planck* data, it has been noticed that the gain between HFI and FIRAS is not constant across the sky: we observe some gain variation (or variation of K, and thus variation of O), that mimics a decrease of K with brightness. Indeed, the calibration given by the narrow part of the Galactic plane and on the lower high latitude gradients differed by 10 to 15 % (see Fig. A.5). To understand this unresolved discrepancy, we had exchanges with the FIRAS team on 1) the FIRAS beam knowledge and its potential changes with frequency; the FIRAS beam is to first order independent of frequency (given by a geometrical optics dominated horn), and 2) non linearity effects. None of these gave a solution to the discrepancy. We also investigated several culprits:

- Pixelisation: FIRAS data and errors are given in the quadrilateralized spherical cube projection[8]. In the nominal pipeline, we computed the calibration gain K reprojecting FIRAS data into HEALPix (using the drizzling method). We have tested reprojecting the HFI data onto the cube (using different schemes for the pixel decimation) to compare HFI data to delivered FIRAS data. We find no difference for the photometric calibration.
- FIRAS beam: the beam is not well known and could result in some variations of K where the signal is rapidly varying on the sky (Galactic plane, molecular clouds, bright cirrus regions). In the HFI calibration, we do not account for FIRAS beam variations with frequencies. But we tested several "beam configurations" to see its impact on the calibration. First, we measured the beam window function B_ℓ using full-sky FIRAS and HFI power spectra. A quite good fit is obtained with a gaussian with a FWHM = 4.°94. We used this beam in the convolution rather than the "nominal beam" to cross-calibrate the two data sets. We also used other FWHMs (4°, 8°, and 10°). We cannot find any beam that reconciles the FIRAS and HFI data.
- Color corrections: To compute K we need to correct the data for the variation of the spectral energy distribution of dust emission across the sky. Working at $\sim$ 7° and having the FIRAS dust spectrum for each pixel, it was easier to compute the color correction at the FIRAS resolution (cc[7°]). However,

$$cc[7^\circ] \int_{7^\circ} S_\nu[5']d\Omega \neq \int_{7^\circ} cc[5']S_\nu[5']d\Omega\,.$$

  We thus checked for several bolometers if the color corrections could produce the spatial variations of K. We used the DR2 all-sky temperature map (from Planck early results. XIX) obtained by fitting HFI+IRIS data with a spectral index equal to 1.8, to compute a color correction map for each HFI pixel. Accordingly, we modify the calibration pipeline to use this cc[5′]. Using cc[5′], a strong variation of K is still observed, which is comparable to the variation observed using cc[7°]. These refined color corrections cannot explain the variation of K across the sky. Note however, that using cc[5′] rather than cc[7°] significantly changes the calibration coefficient for the 545 GHz channels, by 6 % (and not those at 857 GHz).
- Zodiacal Light: The FIRAS data set we are using has the zodiacal emission removed using the *COBE* model. When comparing HFI and FIRAS data, zodiacal residuals are clearly visible in the difference map. We therefore redo the photometric calibration using the HFI data with the zodiacal light removed. The difference [FIRAS − $K \times$ HFI] does not show anymore zodiacal residuals. Removing the zodiacal emission decreases the calibration coefficient by less than 2 % at 857 GHz. However, it does not decrease the observed spatial variations of K.
- Far-side lobes: we finally test if far-side lobes could have any impact on the photometric calibration. For that we consider

[8] Note that Healpix FIRAS data are available on "lambda" but the covariance matrix is not provided

Table A.2. Values computed in the CIB fields (averaged on N1, SP, AG, LH, Bootes and Bootes bis, see Planck Collaboration XVIII (2011) for more details) and expected CIB from Lagache et al. (1999) FIRAS measurements, and from the Béthermin et al. (2012) model, as given in Table 4.

Frequency [GHz]	CIB from HFI [MJy sr^{-1}] (νI_ν = cst)	CIB measured from FIRAS [MJy sr^{-1}] (νI_ν = cst)	CIB from Béthermin et al. (2012) [MJy sr^{-1}] (νI_ν = cst)
857	0.29	0.71±0.23	0.64
545	0.18	0.37±0.12	0.35
353	0.09	0.13±0.04	0.13
217	2.2×10^{-2}	$(3.4\pm1.1)\times10^{-2}$	3.3×10^{-2}

the detectors that have very low far-side lobes contamination (as the 857-2). We noticed that the spatial variation of K is at the same order whatever the FSL contamination.
– Time gain variations: we have searched, unsuccessfully, for any temporal gain variations using the individual calibration of the HFI all-sky survey maps.

We have therefore no other explanation for this effect than a systematic bias in the FIRAS pass4 interstellar dust spectra.

In parallel, converging evidences of an overestimate of the HFI brightness at high frequencies, when calibrating using FIRAS, came to light:

– The SED of sources and diffuse dust were showing an excess at 545 GHz over a smooth interpolation between higher and lower frequencies. Based on a very simple interpolation between the 857 and 353 GHz frequencies, the excess was at the order of 11 %. Using a very simple dust model, a residual dipole was also present in the 545 GHz maps.
– The CMB anisotropies power spectrum is detectable at 545 GHz and the SMICA component separation method showed a 20.3±4.7 % calibration discrepancy. The analysis of the FFP6 simulated datasets showed that the same method gives reliable results at all HFI frequencies.
– The dipole calibration at 545 GHz, although quite uncertain, was also discrepant by ∼20 % with the FIRAS calibration.
– The measurements on planets (Mars, Jupiter, Saturn, Uranus, Neptune) used for beam determination and pointing also showed, for the ones not affected by non linearity effects, excesses for the two sub-millimetre channels with respect to models.

We therefore abandonned the FIRAS calibration to the profit of a planet calibration.

[1] APC, AstroParticule et Cosmologie, Université Paris Diderot, CNRS/IN2P3, CEA/lrfu, Observatoire de Paris, Sorbonne Paris Cité, 10, rue Alice Domon et Léonie Duquet, 75205 Paris Cedex 13, France
[2] Aalto University Metsähovi Radio Observatory, Metsähovintie 114, FIN-02540 Kylmälä, Finland
[3] African Institute for Mathematical Sciences, 6-8 Melrose Road, Muizenberg, Cape Town, South Africa
[4] Agenzia Spaziale Italiana Science Data Center, c/o ESRIN, via Galileo Galilei, Frascati, Italy
[5] Agenzia Spaziale Italiana, Viale Liegi 26, Roma, Italy
[6] Astrophysics Group, Cavendish Laboratory, University of Cambridge, J J Thomson Avenue, Cambridge CB3 0HE, U.K.
[7] Astrophysics & Cosmology Research Unit, School of Mathematics, Statistics & Computer Science, University of KwaZulu-Natal, Westville Campus, Private Bag X54001, Durban 4000, South Africa
[8] Atacama Large Millimeter/submillimeter Array, ALMA Santiago Central Offices, Alonso de Cordova 3107, Vitacura, Casilla 763 0355, Santiago, Chile
[9] CITA, University of Toronto, 60 St. George St., Toronto, ON M5S 3H8, Canada
[10] CNRS, IRAP, 9 Av. colonel Roche, BP 44346, F-31028 Toulouse cedex 4, France
[11] California Institute of Technology, Pasadena, California, U.S.A.
[12] Centre for Theoretical Cosmology, DAMTP, University of Cambridge, Wilberforce Road, Cambridge CB3 0WA U.K.
[13] Centro de Estudios de Física del Cosmos de Aragón (CEFCA), Plaza San Juan, 1, planta 2, E-44001, Teruel, Spain
[14] Computational Cosmology Center, Lawrence Berkeley National Laboratory, Berkeley, California, U.S.A.
[15] DSM/Irfu/SPP, CEA-Saclay, F-91191 Gif-sur-Yvette Cedex, France
[16] DTU Space, National Space Institute, Technical University of Denmark, Elektrovej 327, DK-2800 Kgs. Lyngby, Denmark
[17] Département de Physique Théorique, Université de Genève, 24, Quai E. Ansermet,1211 Genève 4, Switzerland
[18] Departamento de Física Fundamental, Facultad de Ciencias, Universidad de Salamanca, 37008 Salamanca, Spain
[19] Department of Astronomy and Astrophysics, University of Toronto, 50 Saint George Street, Toronto, Ontario, Canada
[20] Department of Astrophysics/IMAPP, Radboud University Nijmegen, P.O. Box 9010, 6500 GL Nijmegen, The Netherlands
[21] Department of Electrical Engineering and Computer Sciences, University of California, Berkeley, California, U.S.A.
[22] Department of Physics and Astronomy, Dana and David Dornsife College of Letter, Arts and Sciences, University of Southern California, Los Angeles, CA 90089, U.S.A.
[23] Department of Physics and Astronomy, University College London, London WC1E 6BT, U.K.
[24] Department of Physics, Gustaf Hällströmin katu 2a, University of Helsinki, Helsinki, Finland
[25] Department of Physics, Princeton University, Princeton, New Jersey, U.S.A.
[26] Department of Physics, University of California, One Shields Avenue, Davis, California, U.S.A.
[27] Department of Physics, University of California, Santa Barbara, California, U.S.A.
[28] Department of Physics, University of Illinois at Urbana-Champaign, 1110 West Green Street, Urbana, Illinois, U.S.A.
[29] Dipartimento di Fisica e Astronomia G. Galilei, Università degli Studi di Padova, via Marzolo 8, 35131 Padova, Italy
[30] Dipartimento di Fisica e Scienze della Terra, Università di Ferrara, Via Saragat 1, 44122 Ferrara, Italy
[31] Dipartimento di Fisica, Università La Sapienza, P. le A. Moro 2, Roma, Italy
[32] Dipartimento di Fisica, Università degli Studi di Milano, Via Celoria, 16, Milano, Italy
[33] Dipartimento di Fisica, Università degli Studi di Trieste, via A. Valerio 2, Trieste, Italy
[34] Dipartimento di Fisica, Università di Roma Tor Vergata, Via della Ricerca Scientifica, 1, Roma, Italy

[35] Discovery Center, Niels Bohr Institute, Blegdamsvej 17, Copenhagen, Denmark
[36] European Southern Observatory, ESO Vitacura, Alonso de Cordova 3107, Vitacura, Casilla 19001, Santiago, Chile
[37] European Space Agency, ESAC, Planck Science Office, Camino bajo del Castillo, s/n, Urbanización Villafranca del Castillo, Villanueva de la Cañada, Madrid, Spain
[38] European Space Agency, ESTEC, Keplerlaan 1, 2201 AZ Noordwijk, The Netherlands
[39] Haverford College Astronomy Department, 370 Lancaster Avenue, Haverford, Pennsylvania, U.S.A.
[40] Helsinki Institute of Physics, Gustaf Hällströmin katu 2, University of Helsinki, Helsinki, Finland
[41] INAF - Osservatorio Astrofisico di Catania, Via S. Sofia 78, Catania, Italy
[42] INAF - Osservatorio Astronomico di Padova, Vicolo dell'Osservatorio 5, Padova, Italy
[43] INAF - Osservatorio Astronomico di Roma, via di Frascati 33, Monte Porzio Catone, Italy
[44] INAF - Osservatorio Astronomico di Trieste, Via G.B. Tiepolo 11, Trieste, Italy
[45] INAF/IASF Bologna, Via Gobetti 101, Bologna, Italy
[46] INAF/IASF Milano, Via E. Bassini 15, Milano, Italy
[47] INFN, Sezione di Bologna, Via Irnerio 46, I-40126, Bologna, Italy
[48] INFN, Sezione di Roma 1, Università di Roma Sapienza, Piazzale Aldo Moro 2, 00185, Roma, Italy
[49] IPAG: Institut de Planétologie et d'Astrophysique de Grenoble, Université Joseph Fourier, Grenoble 1 / CNRS-INSU, UMR 5274, Grenoble, F-38041, France
[50] IUCAA, Post Bag 4, Ganeshkhind, Pune University Campus, Pune 411 007, India
[51] Imperial College London, Astrophysics group, Blackett Laboratory, Prince Consort Road, London, SW7 2AZ, U.K.
[52] Infrared Processing and Analysis Center, California Institute of Technology, Pasadena, CA 91125, U.S.A.
[53] Institut Néel, CNRS, Université Joseph Fourier Grenoble I, 25 rue des Martyrs, Grenoble, France
[54] Institut Universitaire de France, 103, bd Saint-Michel, 75005, Paris, France
[55] Institut d'Astrophysique Spatiale, CNRS (UMR8617) Université Paris-Sud 11, Bâtiment 121, Orsay, France
[56] Institut d'Astrophysique de Paris, CNRS (UMR7095), 98 bis Boulevard Arago, F-75014, Paris, France
[57] Institute for Space Sciences, Bucharest-Magurale, Romania
[58] Institute of Astronomy and Astrophysics, Academia Sinica, Taipei, Taiwan
[59] Institute of Astronomy, University of Cambridge, Madingley Road, Cambridge CB3 0HA, U.K.
[60] Institute of Theoretical Astrophysics, University of Oslo, Blindern, Oslo, Norway
[61] Instituto de Física de Cantabria (CSIC-Universidad de Cantabria), Avda. de los Castros s/n, Santander, Spain
[62] Jet Propulsion Laboratory, California Institute of Technology, 4800 Oak Grove Drive, Pasadena, California, U.S.A.
[63] Jodrell Bank Centre for Astrophysics, Alan Turing Building, School of Physics and Astronomy, The University of Manchester, Oxford Road, Manchester, M13 9PL, U.K.
[64] Kavli Institute for Cosmology Cambridge, Madingley Road, Cambridge, CB3 0HA, U.K.
[65] LAL, Université Paris-Sud, CNRS/IN2P3, Orsay, France
[66] LERMA, CNRS, Observatoire de Paris, 61 Avenue de l'Observatoire, Paris, France
[67] LESIA, Observatoire de Paris, CNRS, UPMC, Université Paris-Diderot, 5 Place J. Janssen, 92195 Meudon, France
[68] Laboratoire AIM, IRFU/Service d'Astrophysique - CEA/DSM - CNRS - Université Paris Diderot, Bât. 709, CEA-Saclay, F-91191 Gif-sur-Yvette Cedex, France
[69] Laboratoire Traitement et Communication de l'Information, CNRS (UMR 5141) and Télécom ParisTech, 46 rue Barrault F-75634 Paris Cedex 13, France
[70] Laboratoire de Physique Subatomique et de Cosmologie, Université Joseph Fourier Grenoble I, CNRS/IN2P3, Institut National Polytechnique de Grenoble, 53 rue des Martyrs, 38026 Grenoble cedex, France
[71] Laboratoire de Physique Théorique, Université Paris-Sud 11 & CNRS, Bâtiment 210, 91405 Orsay, France
[72] Lawrence Berkeley National Laboratory, Berkeley, California, U.S.A.
[73] Max-Planck-Institut für Astrophysik, Karl-Schwarzschild-Str. 1, 85741 Garching, Germany
[74] McGill Physics, Ernest Rutherford Physics Building, McGill University, 3600 rue University, Montréal, QC, H3A 2T8, Canada
[75] National University of Ireland, Department of Experimental Physics, Maynooth, Co. Kildare, Ireland
[76] Niels Bohr Institute, Blegdamsvej 17, Copenhagen, Denmark
[77] Observational Cosmology, Mail Stop 367-17, California Institute of Technology, Pasadena, CA, 91125, U.S.A.
[78] Optical Science Laboratory, University College London, Gower Street, London, U.K.
[79] SB-ITP-LPPC, EPFL, CH-1015, Lausanne, Switzerland
[80] SISSA, Astrophysics Sector, via Bonomea 265, 34136, Trieste, Italy
[81] School of Physics and Astronomy, Cardiff University, Queens Buildings, The Parade, Cardiff, CF24 3AA, U.K.
[82] Space Research Institute (IKI), Russian Academy of Sciences, Profsoyuznaya Str, 84/32, Moscow, 117997, Russia
[83] Space Sciences Laboratory, University of California, Berkeley, California, U.S.A.
[84] Special Astrophysical Observatory, Russian Academy of Sciences, Nizhnij Arkhyz, Zelenchukskiy region, Karachai-Cherkessian Republic, 369167, Russia
[85] Stanford University, Dept of Physics, Varian Physics Bldg, 382 Via Pueblo Mall, Stanford, California, U.S.A.
[86] Sub-Department of Astrophysics, University of Oxford, Keble Road, Oxford OX1 3RH, U.K.
[87] Theory Division, PH-TH, CERN, CH-1211, Geneva 23, Switzerland
[88] UPMC Univ Paris 06, UMR7095, 98 bis Boulevard Arago, F-75014, Paris, France
[89] Université de Toulouse, UPS-OMP, IRAP, F-31028 Toulouse cedex 4, France
[90] University of Granada, Departamento de Física Teórica y del Cosmos, Facultad de Ciencias, Granada, Spain
[91] University of Miami, Knight Physics Building, 1320 Campo Sano Dr., Coral Gables, Florida, U.S.A.
[92] Warsaw University Observatory, Aleje Ujazdowskie 4, 00-478 Warszawa, Poland